

ZnO Coated Nanospring-Based Gas Sensors

A Dissertation

Presented in Partial Fulfill of the Requirements for the

Degree of Doctorate of Philosophy

with a

Major in Physics

in the

College of Graduate Studies

University of Idaho

by

Pavel Viktorovich Bakharev

Major Professor: David N. McIlroy, Ph.D.

Committee Members: You Qiang, Ph.D.; F. Marty Ytreberg, Ph.D.;

Eric Aston, Ph.D.

Department Administrator: Ray von Wandruszka, Ph.D.

July 2015

Authorization to Submit Dissertation

This dissertation of Pavel Viktorovich Bakharev submitted for the degree of Doctorate of Philosophy with a major in Physics and titled “ZnO Coated Nanospring-Based Gas Sensors,” has been reviewed in final form. Permission, as indicated by the signatures and dates given below, is now granted to submit final copies to the College of Graduate Studies for approval.

Major Professor: _____ Date: _____
David N McIlroy, Ph.D.

Committee

Members: _____ Date: _____
You Qiang, Ph.D.

_____ Date: _____
F. Marty Ytreberg, Ph.D.

_____ Date: _____
Eric Aston, Ph.D.

Department

Administrator: _____ Date: _____
Ray von Wandruszka, Ph.D.

Abstract

The current research demonstrates new techniques for characterization of electrical transport properties of the metal oxide polycrystalline structures, gas and vapor phase kinetics, surface processes such as gas-surface, vapor-surface interactions and redox processes by applying novel gas sensing devices. Real-time sensor electrical response characteristics obtained under highly controlled laboratory conditions have been used to characterize corresponding surface interactions and electrical properties of the gas sensitive structures. Novel redox chemical sensors (chemiresistors) have been fabricated with 3-D and 1-D ZnO coated nanospring (NS) structures. Silica NSs served as insulating scaffolding for a ZnO gas sensitive layer and has been grown via a vapor-liquid-solid (VLS) mechanism by using a chemical vapor deposition (CVD) technique. The NSs have been coated with polycrystalline ZnO by atomic layer deposition (ALD). The chemiresistor devices have been thoroughly characterized in terms of their crystal structures (by XRD, FESEM, TEM, and ellipsometry) and their electrical response properties. A 3-D gas sensor has been constructed from a xenon light bulb by coating it with a 3-D zinc oxide coated silica nanospring mat, where the xenon light bulb served as a sensor heater. This inexpensive sensor platform has been used to characterize gas-solid, vapor-solid, and redox processes. The optimal temperature of the gas sensitive ZnO layer, the temperature of the vapor-gas mixture and the crystal structure of the gas sensitive layer have been determined to reach the highest sensitivity of the gas sensors. The activation energy of toluene oxidation (E_a) on the ZnO surface and the activation energy of oxidation (E_a) of the depleted ZnO surface have been determined and analyzed. A 1-D chemiresistor has been fabricated with a single ZnO coated silica nanospring by photolithography. The question of sensor sensitivity of MOS nanomaterials and MOS thin films has been addressed. The

experimental and computational analyses of the sensing properties of the 3-D (nanospring-based) and flat thin films structures show that the complexity and periodic boundary conditions of the nanospring-based devices result in a lower detection limit, while flat thin films exhibit higher sensitivity to small analyte concentration fluctuations. Our analysis shows that the productive approach to fabrication of integrated sensors (electronic noses) is to use both the structures (3D and flat geometries) as the receptors for a prompt and reliable detection and recognition of the target chemical compounds. Analog lock-in amplifier (LIA) AC measurements of the electrical response have been performed to significantly improve the signal-to-noise ratio (SNR) and reduce the detection limit of the single ZnO coated nanospring chemiresistor from the ppm to the ppb analyte concentration ranges. The LIA-based sensor signal recognition technique has shown to extend the capabilities of the gas sensor array for a linear discrimination analysis (LDA), an independent component analysis (ICA), a principal component analysis (PCA) and other multiple odor recognition methods.

Acknowledgments

I would like to express my sincere gratitude to Dr. David N. McIlroy, my major professor, for admitting me into his research group as well as for his patience in supporting and leading me through challenging experimental research assignments. I will adhere to his values and ideals as a skillful researcher throughout my career.

I am thankful to the committee members Dr. You Qiang, Dr. F. Marty Ytreberg and Dr. D. Eric Aston for their time and suggestions. I would like to thank the Department of Physics and the University of Idaho for providing an invaluable opportunity and an inspiring working environment to pursue my research objectives.

I am happy to express my gratitude to Dr. Giancarlo Corti for teaching me the in-depths of micro/nanofabrication methods and working with equipment in the micro and nanotechnology cleanroom facility at the University of Idaho.

I would like to thank all the Physics Department faculty and staff, especially Mr. John Faila who is an amazing professional in machining and engineering that enabled us to build custom-built equipment.

Finally, I would like to acknowledge the financial support of the Office of Navy Research (ONR), the National Institute for Advanced Transportation Technology (NIATT), and the College of Science's Dyess Faculty Fellowship.

Pavel V. Bakharev

Physics Department, University of Idaho

Moscow, ID, 83844-0903

Table of Contents

Authorization to Submit Dissertation	ii
Abstract.....	iii
Acknowledgements.....	iv
Table of Contents.....	v
List of Figures.....	vii
CHAPTER 1: Introduction	1
1.1 Sensor Application of Nanomaterials.....	1
1.2 Metal Oxide Semiconductor Gas Sensors	3
1.3 Zinc Oxide Based Gas Sensors.....	6
1.4 Gas Sensor Applications: Practical and Fundamental	7
1.5 Overview of the Study	8
References.....	9
CHAPTER 2: ZnO Coated Nanospring Mat-Based Chemiresistor.....	13
Abstract.....	13
2.1 Introduction.....	14
2.2 Material Preparation	15
2.2.1 Silica Nanospring Mat Synthesis.....	15
2.2.2 Atomic Layer Deposition of ZnO.....	19
2.3 Electrical Characterization.....	22
2.4 Results.....	24
2.5 Discussion.....	27
2.6 Conclusions.....	35

References.....	36
CHAPTER 3: Single ZnO Coated Nanospring Chemiresistor; Influence of Chemiresistor Geometry on its Response Properties.....	41
Abstract.....	41
3.1 Introduction.....	42
3.2 Experimental Section.....	43
3.2.1 ZnO Coated Nanospring Separation.....	45
3.2.2 Photolithography.....	46
3.2.3 Electrical Characterization.....	49
3.3 Results and Discussion	51
3.4 Computational Model	57
3.5 Conclusions.....	63
References.....	65
CHAPTER 4: DC vs. Lock-in Amplifier AC Electrical Response Measurements.....	69
Abstract.....	69
4.1 Introduction.....	70
4.2 Experimental Section.....	71
4.2.1 DC Measurements	71
4.2.2 Lock-in Amplifier AC Measurements	74
4.3 Conclusions.....	81
References.....	82
CHAPTER 5: Summary	86
5.1 Conclusions.....	86

5.2 Future Directions	87
Appendix:	88

List of Figures

Figure 1.1: Schematic representation of (a) receptor/transducer/signal model and (b) gas sensor structure.	2
Figure 1.2: Schematics of energy band configurations, potential barriers and electrical properties of MOS polycrystalline structure upon surface redox and catalytic analyte (toluene) oxidation processes. E_c and E_v are the lowest edge of the conduction band and the highest edge of the valence band, respectively; E_F is the Fermi level in the n-type MOS; E_i represents the energy levels corresponding to defect states in MOS.	5
Figure 2.1: (a) – (d) Schematic representation of silica nanowire/nanospring growth via vapor-liquid-solid process. (e) SEM image of silica nanosprings.	15
Figure 2.2: SEM micrographs of (a) a silica nanospring mat, (b) of ZnO coated nanosprings. (c) A XRD spectrum of ZnO coated nanosprings.	20
Figure 2.3: (a) Schematic of the ALD system utilized for ZnO deposition. (b) The variation of the chamber pressure during each cycle.	21
Figure 2.4: (a) A schematic of the experimental setup used to acquire electrical response of the xenon light bulb chemiresistor, (b) the xenon light bulb sensor and (c) the light bulb sensor mounted in the jig.	23
Figure 2.5: The relative changes in resistance of the light bulb ZnO nanospring sensor at (a) $T_{LB} = 280^\circ\text{C}$, (b) $T_{LB} = 370^\circ\text{C}$, and (c) $T_{LB} = 435^\circ\text{C}$ upon exposure to sequential 1000 ppm toluene pulses at fixed vapor-gas temperature $T_V = 22^\circ\text{C}$	26
Figure 2.6: The relative changes in resistance of the xenon light bulb ZnO nanospring sensor upon exposure to 1000 ppm consequent toluene pulses at different vapor gas mixture temperatures T_V and the optimal light bulb temperature $T_{LB} = 435^\circ\text{C}$. (a) $T_V = 100^\circ\text{C}$, (b) $T_V = 200^\circ\text{C}$, (c) $T_V = 250^\circ\text{C}$,	

and (d) $T_V = 300^\circ\text{C}$27

Figure 2.7: (a) Exponential ‘RC-circuit’ approximation of the sensor response. Energy level schematics (b) of the bulk ZnO, (c) at the depleted surface of ZnO, and (d) upon toluene oxidation on the ZnO surface (arbitrary intrinsic E_i levels correspond to defect states in n-type ZnO). Schematic energy-level diagrams of the polycrystalline ZnO layer (e) prior to toluene exposure and (f) after exposure and subsequent toluene oxidation.28

Figure 2.8: (a) The average baseline resistance of the xenon light bulb ZnO nanospring sensor ($T_{LB}=435^\circ\text{C}$) at different vapor gas mixture temperatures T_V . (b) The average change in the chemiresistor response to 1000 ppm toluene vapor at different vapor gas mixture temperatures T_V ($T_{LB}=435^\circ\text{C}$).33

Figure 3.1: XRD spectra of (a) ZnO coated nanosprings and (b) the ZnO layer on the surface of SiO_2 wafer.44

Figure 3.2: Schematics of ZnO coated nanospring separation and their transfer onto a glass substrate.45

Figure 3.3: A schematic representation of a step-by-step procedure of making Ti–Au ohmic contacts by photolithography.47

Figure 3.4: (a) individual ZnO coated nanosprings with applied Ti–Au electrodes. (b) Schematic representation of a single nanospring device.48

Figure 3.5: (a) Schematic of the two-probe measurement system used to acquire electrical response of individual ZnO coated silica nanospring. (b) I-V characteristics of a single ZnO coated nanospring device and of the electrodes without nanospring at temperature of 300°C50

Figure 3.6: The relative changes in resistance of a single ZnO coated nanospring sensor upon exposure to 1000 ppm consequent pulses of toluene

vapor at different sensor temperatures T_{NS} (the vapor gas mixture temperature T_V was set around the room temperature). (a) $T_{NS}=160^\circ\text{C}$, (b) $T_{NS}=270^\circ\text{C}$, (c) $T_{NS}=310^\circ\text{C}$, and (d) $T_{NS}=350^\circ\text{C}$52

Figure 3.7: The relative changes in resistance of a single ZnO coated nanospring sensor upon exposure to 1000 ppm consequent pulses of toluene vapor at different vapor gas mixture temperatures T_V . The sensor temperature $T_{NS}=310^\circ\text{C}$. (a) $T_V=200^\circ\text{C}$, (b) $T_V=250^\circ\text{C}$, and (c) $T_V=300^\circ\text{C}$54

Figure 3.8: (a) The relative changes in resistance of a single ZnO coated nanospring sensor upon exposure to toluene vapor at 60 ppm, 40 ppm, and 20ppm, (b) the relative changes in resistance of a ZnO thin film on a flat SiO_2 surface upon exposure to toluene vapor at 60 ppm, 40 ppm, and 20 ppm and (c) the linear extrapolations of the responses of a single ZnO coated nanospring chemiresistor and the ZnO thin film chemiresistor as a function of toluene concentration.....55

Figure 3.9: Schematics of a hexagonal polycrystalline MOS structure grown with c -axis orientation (top view).58

Figure 3.10: Schematics of hexagonal polycrystalline structure with a (002) orientation and its equivalent electrical circuit.60

Figure 3.11: Numerical simulations of the relative changes of the measured resistances δR_{net} as functions of N for hexagonal polycrystalline structure on flat and arbitrary 3D structures at different δR_{ij} . (a) $\delta R_{ij}=0.1$, (b) $\delta R_{ij}=0.05$, (c) $\delta R_{ij}=0.01$. (d) Linear approximations of δR_{net} as functions of δR_{ij} for 3D at $N=0.024$ and flat structures.62

Figure 4.1: DC electrical response of a single ZnO coated nanospring sensor. The relative changes in resistance upon exposure to toluene vapor at (a) 60 ppm, 40 ppm, 20 ppm, and (b) 10 ppm.....72

Figure 4.2: A schematic of the gas sensor test station utilized to perform

lock-in amplifier AC measurements.....75

Figure 4.3: (a) Schematic of the lock-in based experimental set-up utilized for toluene vapor detection. (b) Layout of signal pathway through an analog lock-in amplifier (LIA). The symbols Σ and \times represent summing and mixing (multiplying) stages, respectively. PSD and LPF are a multiplier, called the phase sensitive detector, and a low-pass filter with transfer function $H(\omega)$, respectively.....77

Figure 4.4: The electrical response of a single ZnO coated nanospring device measured at lock-in amplifier (LIA) output upon exposure to toluene vapor at (a) 60 ppm, (b) 40 ppm, (c) 20 ppm, and (d) 10 ppm.79

Figure 4.5: Signal-to-noise ratios (SNRs) in decibel scale of a single ZnO coated nanospring sensor obtained by utilizing the DC and the analog lock-in amplifier (LIA) modes of detection.....80

CHAPTER 1

Introduction

1.1 Sensor Application of Nanomaterials

A chemical sensor is a device that transforms chemical information (concentration, composition, partial pressure, etc.) of an analyte present in the designated environment into an analytically useful signal (typically electric or optical signals). In general, sensors contain two main parts in series, namely, a chemical recognition system (receptor) and a transducer (Fig. 1.1 a). The receptor interacts with analyte species converting the chemical information into a form of energy, which can be measured by the transducer. The transducer converts this energy into analytical signals, which can be electrical or optical among others.

In general, sensors can be subdivided into physical sensors, chemical sensors, and biochemical sensors [1]. Physical sensors produce analytical signals in response to physical processes, such as mass, absorbance, refractive index, temperature, or conductivity change. Chemical sensors provide analytical information about chemical composition of analytes. The sensing mechanism of this type of sensors is based on chemical interactions (reactions) between analyte species and the sensor receptor. Biochemical sensors are a subclass of chemical sensors, which are used to detect and recognize biological components, such as cells, proteins, nucleic acids, *etc.* It is often impossible to distinguish between physical and chemical sensors, as is in the case of a gas sensor in which the signal is a result of gas adsorption.

Typically, a gas sensing device consists of the following main components (see Fig. 1.1 b):

- Gas sensitive layer (receptor)

- Substrate (which is a scaffolding for the sensitive layer)
- Electrodes
- Heating element

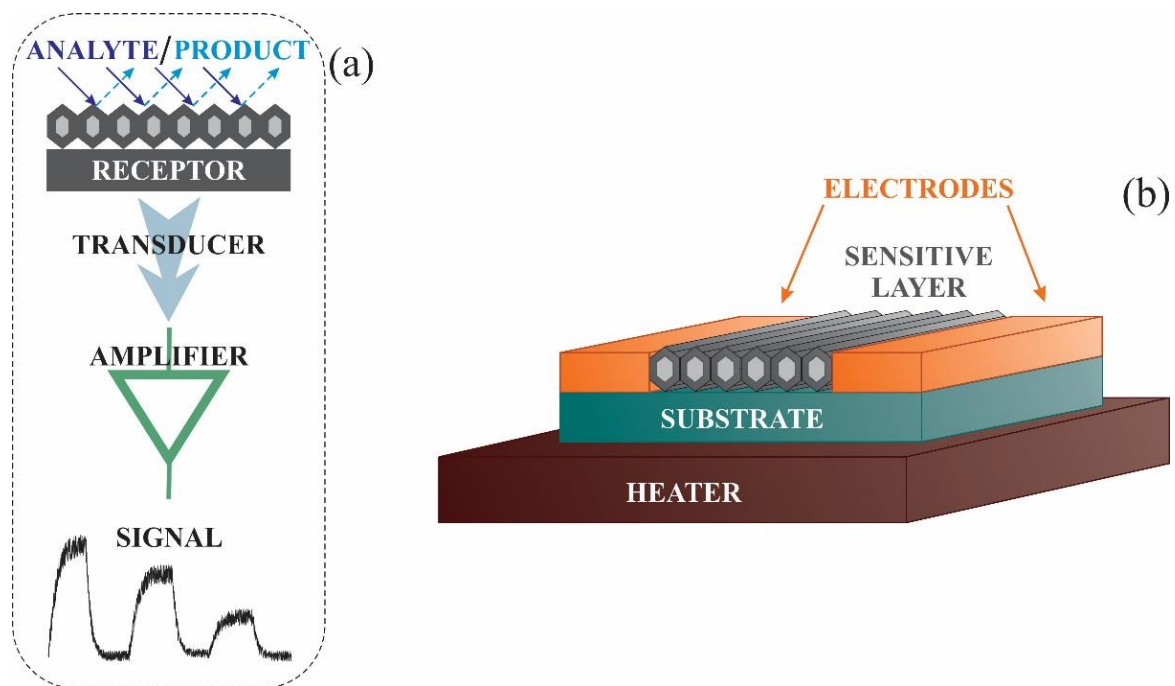


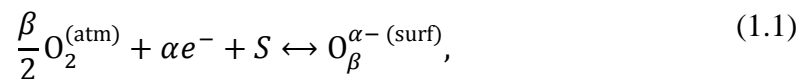
Figure 1.1 Schematic representation of (a) receptor/transducer/signal model and (b) gas sensor structure.

It is critical for practical applications that the gas sensor systems should be compact, portable devices, which are able to promptly and reliably detect and recognize analyte compounds. The power consumption of gas sensors should be as low as possible and the heat losses corresponding to conduction, convection or the heater radiation should be minimized. Obviously enough, miniaturization of the gas sensing elements by utilizing the recent micro- and nanofabrication techniques [2–7] is the only way to meet these requirements.

The nanoscale gas sensors demonstrate higher sensitivity, lower detection limit, shorter response and recovery times, wider dynamic range (analyte concentration range between the detection limit and the highest limiting concentration of a sensor), lower working temperature, and more heat shock resistant than their macro-counterparts. The nanomaterials are very susceptible to changes at their surfaces due to the fact that the characteristic length scales of the surface interactions are comparable to the dimensions of the nanomaterials. Hence, sensing is one of the most advantageous application of nanostructures [1–14].

1.2 Metal Oxide Semiconductor Gas Sensors

Nowadays, metal oxide semiconductors (MOSs) are widely used for detection and recognition of a vast range of gases and vapors. Typically, the analytes of interest include hydrocarbons, alcohol vapors, carbon oxides, nitrogen oxide, hydrogen, ammonia, vapors of explosives and their residues, etc. Nanoscale MOSs, such as polycrystalline 2-D nanostructures of ZnO, TiO₂, SnO₂ currently dominate as sensitive layers in gas sensors due to the fact that these n-type semiconductor materials at moderately elevated temperature adsorb atmospheric oxygen to form a reactive surface ‘layer’ of O₂⁻, O⁻ and O²⁻ species. In terms of the electrical properties, the formation of the ionized molecular (O₂⁻) and atomic (O⁻, O²⁻) species at the surface indicates that the n-type MOS thin films are highly susceptible to the catalytic oxidations of the gaseous analyte compounds at their surfaces. As a result, the MOS nanostructures are commonly utilized as gas sensitive layers in chemiresistors [1–14]. It has been reported [12–14] that at the MOS temperature below 150°C the molecular form of oxygen prevails, while above 150°C the ionic oxygen species dominates. In general, the surface oxidation/reoxidation (redox) process can be described by the reaction [1]



where $O_2^{(\text{atm})}$ and $O_{\beta}^{\alpha-}(\text{surf})$ are an oxygen molecule in the ambient atmosphere and the chemisorbed oxygen, respectively; e^- denotes the electrons from the near surface MOS region that can reach the oxygen species at the surface; S indicates unoccupied oxygen surface sites; coefficients $\alpha=1$ or 2 and $\beta=1$ or 2 correspond to the singly or doubly ionized and to atomic or molecular oxygen forms, respectively. The oxygen chemisorption process leads to the formation of the negative surface charge that depletes the n-type MOS layer, subsequently increasing the electrical resistance of the gas sensitive layer. The self-refreshing reoxidation of the surface enables the MOS-based chemiresistor to return to its baseline conditions. The discussion of the depletion layer formation and the general relations for the surface charge, the surface potential barrier, the characteristic depletion and the Debye lengths will be given in Chapter 2.

The electrical response to the analyte vapor present in the ambient atmosphere is attributed to the catalytic oxidation of the target compound at the MOS surface and corresponding stripping of chemisorbed oxygen species from the surface. In turn, this reduces the surface charge and increases the conductance of the MOS gas sensitive layer.

The reaction equation for the analyte oxidation process depends on the type of the target gas or vapor. For example, the catalytic oxidation of toluene vapor can be expressed in the form of two different reactions. The first reaction is dehydrogenation of toluene ($C_6H_5CH_3$) to benzaldehyde (C_7H_6O), and the second reaction is the oxidation of benzaldehyde to benzoic acid ($C_7H_6O_2$) [15–17]

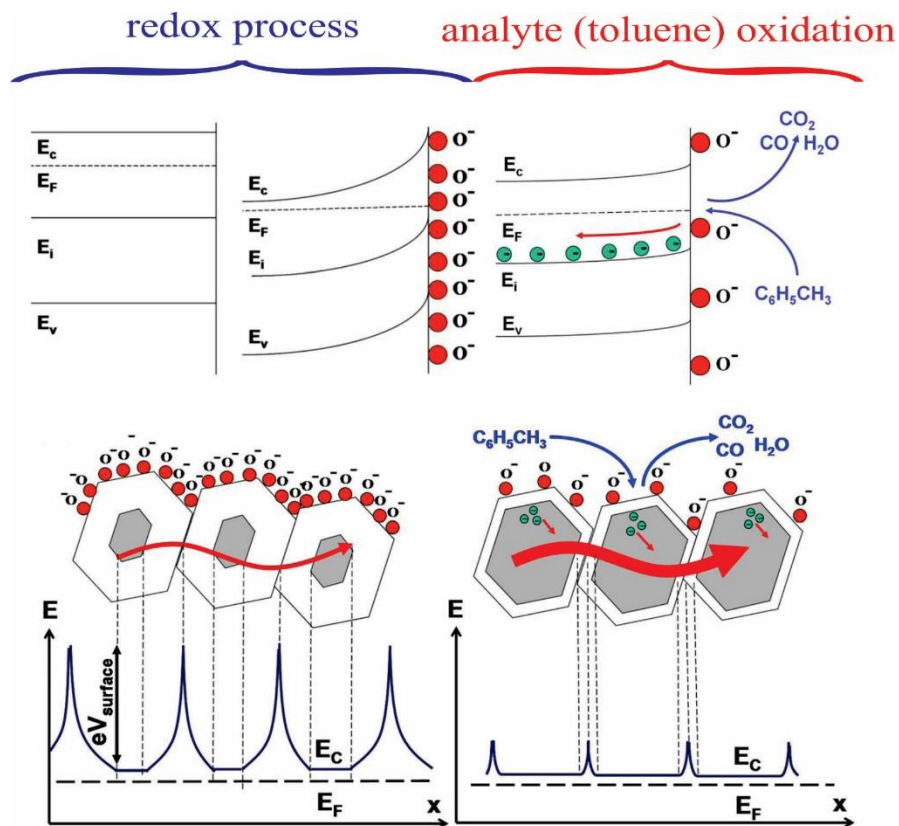
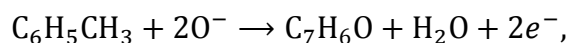
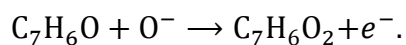


Figure 1.2 Schematics of energy band configurations, potential barriers and electrical properties of MOS polycrystalline structure upon surface redox and catalytic analyte (toluene) oxidation processes. E_c and E_v are the lowest edge of the conduction band and the highest edge of the valence band, respectively; E_F is the Fermi level in the n-type MOS; E_i represents the energy levels corresponding to defect states in MOS.



(1.2)



The self-refreshing reoxidation (redox) and catalytic analyte (toluene) oxidation processes at the surface and their influence on the energy band configurations, the potential barriers, and the electron transport properties of the polycrystalline MOS structure can be schematically illustrated as shown in Fig. 1.2.

1.3 Zinc Oxide Based Gas Sensors

Zinc oxide (ZnO) is a II-VI semiconductor group compound with a relatively wide direct band gap of approximately 3.4 eV at room temperature [18]. Under usual preparation techniques and conditions, the ZnO semiconductor is n-type due to oxygen vacancies or zinc interstitials, which act as the native donor [19]. The zinc excess leads to the formation of a non-stoichiometric compound $Zn_{1+\delta}O$ and to a structural disorder in crystal structure [20]. This MOS has several important properties such as good transparency, high electron mobility, and strong room temperature luminescence. ZnO is widely used in gas sensor applications (as gas sensitive layers), in piezoelectric devices, in surface acoustic wave (SAW) devices, as UV resistive material, as transparent conductive metal oxide electrodes, etc.

Outstanding gas sensing properties of ZnO nanostructures are attributed to the fact that the surface of $Zn_{1+\delta}O$ is oxygen deficient and at elevated temperature readily oxidized in ambient atmosphere to result in the surface stoichiometry of ZnO. The chemisorption and further dissociation of oxygen on defect sites, such as oxygen vacancies or interstitial zinc ions, makes zinc oxide a highly sensitive material to typical MOS gaseous target compounds. In addition to the excellent gas sensing properties, ZnO nanostructures are attractive due to the various techniques currently available for their synthesis [3,4,6,10,11,21–25].

1.4 Gas Sensor Applications: Practical and Fundamental

The recent techniques in synthesis of nanostructures, such as atomic layer deposition (ALD) [3,4,10,22,23], chemical vapor deposition (CVD) [25–27], vapor-liquid-solid (VLS) method [2,28,29], physical vapor deposition (PVD) [5,21,24], etc. [6,8] allow one to precisely control the dimensions, shape and crystal structures of nanomaterials. On the one hand, the current nanostructures synthesis methods enable one to empirically determine the optimal gas sensor parameters for particular target compounds. The conductometric gas sensors are widely used for monitoring the concentrations of compounds in industrial processes, for environmental applications, and for detection of hazardous gases and vapors. On the other hand, the nanoscale gas sensing systems of different geometries with specific crystal structure characteristics (thickness, crystal planes orientations, grain size, etc.) are necessary for fundamental understanding of the corresponding chemical and physical processes, such as gas-solid, vapor-solid, redox processes, for studying the influence of the sensitive layer geometry on its electron transport properties and, hence, on electrical response characteristics.

The chemisorption of oxygen and catalytic oxidation of various analytes on MOS surfaces have been intensively studied by many groups. However, there is still a strong need for developing new simple methods for the quantitative characterization of these processes, e.g., in terms of activation energies of corresponding adsorption, desorption and catalytic oxidation processes. In Chapter 2 of the current dissertation, we propose a new approach to the quantitative characterization of the aforementioned processes based on the analysis of the real time electrical sensor responses.

In the last decade, various gas sensor platforms of different geometries synthesized by utilizing numerous fabrication techniques have been invented. While the structural, gas

reactive, electrical, optical properties and sensing mechanisms of the sensor devices have received thorough consideration, the influence of the chemiresistor geometry on its performance characteristics still needs to be addressed. In Chapter 3 we conduct a comparison of the electrical response characteristics of the ZnO thin film with those characteristics of ZnO coated nanospring based device.

1.5 Overview of the Study

In the current dissertation, Chapter 2 is devoted to the synthesis and thorough characterization of a novel inexpensive redox chemiresistor constructed from a xenon light bulb by coating it with a 3-D zinc oxide coated silica nanospring mat. This gas sensor served as a platform for qualitative and quantitative characterization of gas-solid, vapor-solid, gas-vapor, and redox processes. In Chapter 3, the MEMS gas sensor (a single ZnO coated nanospring chemiresistor) and its gas sensing properties are studied. The comparison of the electron transport properties of MOS coated 3D structures with those of MOS thin films, as well as the influence of the sensor geometry on its gas sensing properties are presented in Chapter 3. The description of the noise sources in chemiresistor gas sensors, the method for significant increase of the signal-to-noise ratio in sensor response, and comparison of the DC and analog lock-in amplifier AC measurements are reported in Chapter 4. Finally, Chapter 5 is a summary of the study.

References

- [1] Bochenkov, V.; Sergeev, G. Sensitivity, Selectivity, and Stability of Gas-sensitive Metal-oxide Nanostructures. In *Metal Oxide Nanostructures and Their Applications*, 2nd ed.; Umar, H., Ed.; American Scientific Publishers: Stevenson Ranch, CA, USA; Volume 3, pp. 31–52 (2010).
- [2] Choi, Y.-L.; Hwang, S.; Park, J.-G.; Choi, K.; Park, J.-H.; Lee, J.-H. Novel Fabrication of an SnO₂ Nanowire Gas Sensor with High Sensitivity. *Nanotechnology*, 19, 095508 (2008).
- [3] Dobrokhotov, V., *et al.* ZnO Coated Nanospring-Based Chemiresistor. *J. Appl. Phys.*, 111, 044311:1–044311:8 (2012).
- [4] Bakharev, P.; Dobrokhotov, V.; McIlroy, D. A Method for Integrating ZnO Coated Nanosprings into a Low Cost Redox-Based Chemical Sensor and Catalytic Tool for Determining Gas Phase Reaction Kinetics. *Chemosensors*, 2, 56–68 (2014).
- [5] Karunagaran, B., *et al.* TiO₂ Thin Film Sensor for Monitoring Ammonia. *Materials Characterization*, 58, 680–684 (2007).
- [6] Wöllenstein, J., Plaza, JA., Cané, C., Min, Y., Böttner, H., Tuller, HL. A novel single chip thin film metal oxide array. *Sensors and Actuators B*, 93, 350–355 (2003).
- [7] Sadedhian, R.; Kahrizi, M. A Novel Gas Sensor Based on Tunneling-Field-Ionization on Whisker-Covered Gold Nanowires. *IEEE Sensors Journal*, VOL. 8, 2, 161–169 (2008).
- [8] Shen, G.; Chen, P.-C.; Ryu, K.; Zhou, C. Devices and Chemical Sensing Applications of Metal Oxide Nanowires, *Journal of Materials Chemistry*, 19, pp. 828–839 (2009).

- [9] Gouma, P. Nanostructured Polymorphic Oxides for Advanced Chemosensors, *Rev. Adv. Mater. Sci.*, 5, pp. 123-138 (2003).
- [10] Bakharev, P.; McIlroy, D. The effect of the periodic boundary conditions of a ZnO-coated nanospring on its surface redox-induced electrical response. *Nanotechnology*, 2014, 25, 475501 (2014).
- [11] Ra H, Khan R, Kim J, Kang B, Im Y. The effect of grain boundaries inside the individual ZnO nanowires in gas sensing. *Nanotechnology*, 21, doi:10.1088/0957-4484/21/8/085502 (2010).
- [12] Barsan, N.; Weimar, U. Conduction model of metal oxide gas sensors. *J. Electroceramics*, 7, 143–167 (2001).
- [13] Gurlo, A.; Bârsan, N.; Oprea, A.; Sahm, M.; Sahm, T.; Weimar, U. An n- to p-type conductivity transition induced by oxygen adsorption on α -Fe₂O₃. *Appl. Phys. Lett.*, 85, doi:10.1063/1.1794853 (2004).
- [14] Barsan, N.; Schweizer-Berberich, M.; Gopel, W. Fundamental and practical aspects in the design of nanoscaled SnO₂ gas sensors: a status report. *Fresenius' journal of analytical chemistry*, 365, pp. 287–304 (1999).
- [15] Zhang, T.; Mao, L.; Liu, W. Gas phase selective catalytic oxidation of toluene to benzaldehyde on V₂O₅-Ag₂O-Al₂O₃ catalyst. *Journal of Natural Gas Chemistry*, 13, pp. 238–243 (2004).
- [16] Saqer, S.; Kondarides, D.; Verykios, X. Catalytic activity of supported platinum and metal oxide catalysts for toluene oxidation, *Topics in Catalysis*, 52, pp. 517–527 (2009).

- [17] Boikov, E.; Vishnetskaya, M.; Emel'yanov, A.; Tomskii, I.; Shcherbakov, N. The selective catalytic oxidation of toluene, *Russian Journal of Physical Chemistry A*, 82, pp. 2233–2237 (2008).
- [18] Huang, M.; Mao, S.; Feick, H.; Yan, H.; Wu, Y.; Kind, H.; Weber, E.; Russo, R.; Yang, P. Room-temperature ultraviolet nanowire nanolasers. *Science*, 292, pp. 1897–1899 (2001).
- [19] Özgür, Ü.; Alivov, Ya. I.; Liu, C.; Teke, A.; Reshchikov, M. A.; Doğan, S.; Avrutin, V.; Cho, S.-J.; Morkoç, H. A comprehensive review of ZnO materials and devices. *Journal of Applied Physics*, 98 (4): 041301 (2005).
- [20] Hirschwald, W.; *et al.* Zinc oxide. In *Current Topics in Materials Science*. Kaldis, E., Ed.; North-Holland Publishing Company; Volume 7, pp. 153–168 (1981).
- [21] Min, Y.; Tuller, H.; Palzer, S.; Wöllenstein, J.; Böttner, H. Gas response of reactively sputtered ZnO films on Si-based micro array. *Sensors and Actuators B*, 93, pp. 435–441 (2003).
- [22] Przeździecka, E. Characterization of ZnO films grown at low temperature. *Acta Phys. Pol. A*, 114, pp. 1303–1310 (2008).
- [23] Guziewicz, E. ZnO by ALD-advantages of the material grown at low temperature. *Acta Phys. Pol. A*, 116, pp. 814–817 (2009).
- [24] Li, Q.H.; Gao, T.; Wang, Y.G.; Wang, T.H. Adsorption and desorption of oxygen probed from ZnO nanowire films by photocurrent measurements. *Appl. Phys. Lett.*, 86, 123117:1–123117:3 (2005).
- [25] Wan, H.; Ruda, H. A study of the growth mechanism of CVD-grown ZnO nanowires. *Journal of Materials Science Materials in Electronics*, 21(10), pp. 1014–1019 (2010).

- [26] Jeong, J.; Choi, S.P.; Hong, K.J.; Song, H.J.; Park, J.S. Structural and optical properties of SnO₂ thin films deposited by using CVD techniques. *Journal of the Korean Physical Society*, Vol. 48, No. 5, pp. 960–963 (2006).
- [27] Mills, A.; Elliott, N.; Parkin, I.; O'Neill, S.; Clark, R. Novel TiO₂ CVD films for semiconductor photocatalysis. *Journal of Photochemistry and Photobiology A: Chemistry*, Vol. 151, Issues 1–3, pp. 171–179 (2002).
- [28] McIlroy, D.N.; Alkhateeb, A.; Zhang, D.; Aston, D.E.; Marcy, A.C.; Norton, M.G. Nanospring formation—Unexpected catalyst mediated growth. *J. Phys. Condens. Matter*, 16, R415–R440 (2004).
- [29] Wang, L.; Major, D.; Paga, P.; Zhang, D.; Norton, M.G.; McIlroy, D.N. High yield synthesis and lithography of silica-based nanospring mats. *Nanotechnology*, 17, S298–S303 (2006).

CHAPTER 2

ZnO Coated Nanospring Mat-Based Chemiresistor

Bakharev, P.; Dobrokhotov, V.; McIlroy, D. A method for integrating ZnO coated nanosprings into a low cost redox-based chemical sensor and catalytic tool for determining gas phase reaction kinetics. *Chemosensors*, 2014, 2, 56–68.

Abstract

A chemical sensor (chemiresistor) was constructed from a xenon light bulb by coating it with a 3-D zinc oxide coated silica nanospring mat, where the xenon light bulb serves as the sensor heater. The sensor response to toluene as a function of xenon light bulb sensor temperature (T_{LB}) and vapor temperature (T_V) was observed and analyzed. The optimum operational parameters in terms of T_{LB} and T_V were determined to be 435°C and 250°C, respectively. The activation energy of toluene oxidation (E_d) on the ZnO surface was determined to be 87 $\text{kJ}\cdot\text{mol}^{-1}$, while the activation energy of oxidation (E_a) of the depleted ZnO surface was determined to be 83 $\text{kJ}\cdot\text{mol}^{-1}$. This study serves as proof of principle for integrating nanomaterials into an inexpensive sensor platform, which can also be used to characterize gas-solid, or vapor-solid, redox processes.

2.1 Introduction

It is of the utmost interest to develop conductometric gas sensors, which are electronic devices for converting chemical information about the analyte into an analytically useful electrical, or optical, signal. There are a number of reasons for this interest. On the one hand, they can be used for monitoring the concentrations of components in industrial processes, for environmental applications, for detection of hazardous materials (e.g. explosives vapors), etc. On the other hand, these devices are necessary for acquiring a fundamental understanding of corresponding physical and chemical processes triggered by surface-molecule interactions (chemisorption), as well as for interpreting the electrical transport properties of gas sensitive materials. The use of metal oxide nanocrystalline thin films, as well as other more complex nano-morphologies, as the gas sensitive layers in chemiresistors is well documented [1–11]. These studies demonstrated that if the dimensions of the nanostructures are comparable to the characteristic length scales of surface interactions, the sensor will be more responsive to changes in surface stoichiometry. In chemiresistors the catalytic oxidation of analyte at the metal oxide surface depletes the surface of oxygen, which leads to a change in the surface depletion layer. If the depletion layer is comparable to the dimensions of the nanostructured metal oxide, small changes in the depth of the surface depletion layer can produce large swings in the resistivity of the chemiresistor [1–11].

In this chapter we demonstrate a method for constructing an inexpensive chemiresistor using ZnO coated silica nanosprings. The chemiresistor consists of a conventional xenon light bulb, readily purchased at a hardware store, coated with nanosprings, which in turn, are coated with ZnO. The xenon bulb is the heat source to activate electron hopping conduction in the ZnO, as well as the thermal energy need to oxidize the analyte. The mat of ZnO coated silica

nanosprings is an ultra-high surface area material ideally suited for detecting gas-surface and vapor-surface interactions. In addition to being a sensor, it can be used for qualitative and quantitative characterization of gas-solid and vapor-solid interactions, as well as redox processes.

2.2 Material Preparation

2.2.1 Silica Nanospring Mat Synthesis

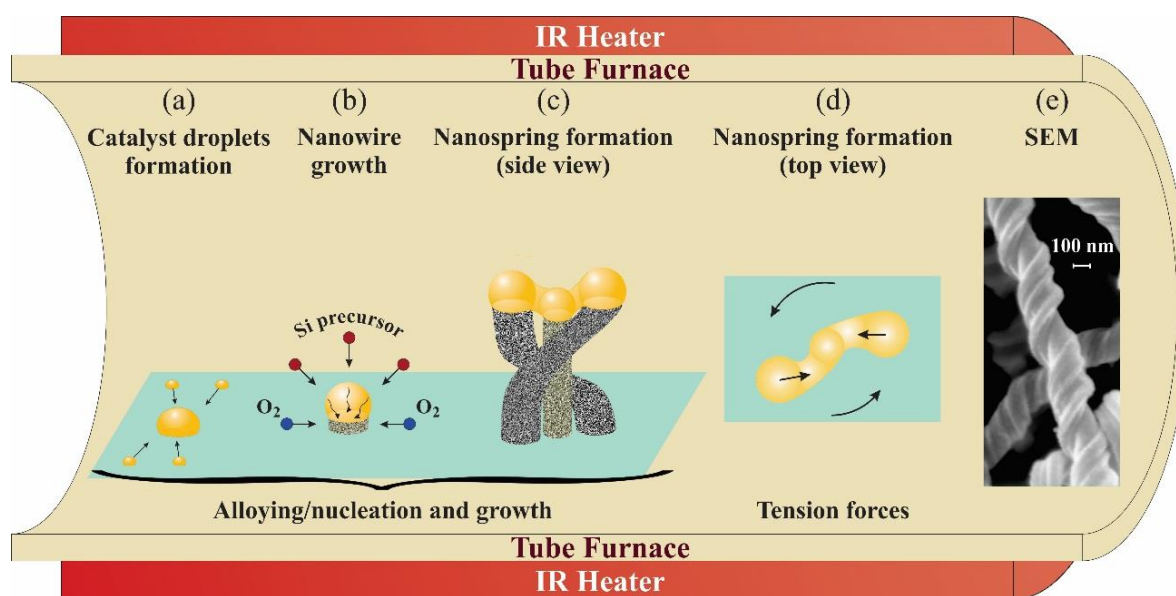


Figure 2.1 (a) – (d) Schematic representation of silica nanowire/nanospring growth via vapor-liquid-solid process. (e) SEM image of silica nanosprings.

In our study, silica (SiO₂) nanosprings (NSs), used as scaffolding for the gas sensitive polycrystalline ZnO layer, were synthesized via the vapor-liquid-solid (VLS) mechanism. VLS growth of SiO₂ NSs by chemical vapor deposition (CVD) was performed in a 3-zone tube furnace with infrared (IR) lamp-heated central zone operated at atmospheric pressure

[12]. A gold layer of approximately 5 nm thickness sputtered onto the surface of the light bulb served as the catalyst for the VLS process. The light bulb was then placed in the tube furnace held at approximately 350°C under a constant flow of O₂ and a proprietary silicon precursor [US patent application 11/993452, filed 2010]. The NS VLS growth proceeds through the following steps (schematically shown in Fig. 2.2):

- *Gold catalyst droplets formation* - When heated, the gold thin layer breaks up and liquid nanodroplets are formed. These droplets diffuse into larger droplets (Fig. 2.1 (a)) and when the radii of the agglomerated droplets exceed the metal droplet minimum radius, R_{\min} , the nanowire (NW) growth can be initiated. Thermodynamically, the minimum metal droplet radius is given by

$$R_{\min} = \frac{2V_L}{RT \ln(s)} \sigma_{LV}, \quad (2.1)$$

where V_L is the molar volume of the droplet, σ_{LV} is the liquid-vapor surface energy, and s is the degree of vapor-phase supersaturation [13– 15]. Equation (2.1) restricts the minimum size of metal droplets needed for NW/NS growth in the VLS process.

- *Nanowire growth* - The agglomerated gold droplets absorb Si precursor vapor to supersaturation level, at this point NW is initiated at the liquid alloy–solid interface (nucleation). The silicon oxidation process takes place at the NW tip–catalyst droplet interface resulting in the formation of the silica NW (Fig. 2.2 (b)). The NW growth kinetics and the growth rate, v , are determined by the thermodynamic quantity $\Delta\mu$, called supersaturation, which is the chemical potential difference of the growth component species in the vapor phase and the solid crystal phase [16–18]. Based on

the classical crystal growth kinetics theory [18], the growth velocity, v , of the NW has a quadratic dependence on the supersaturation, $\Delta\mu$:

$$v = \gamma \left(\frac{\Delta\mu}{kT} \right)^2, \quad (2.2)$$

where γ is the kinetic coefficient of growth at the solid-liquid interface. In the case of the synthesis of the nanoscale structure with high surface-to-volume ratio, the surface energy of the nanostructure has a significant effect on its thermodynamic growth process. In the frames of the Gibbs-Thompson approach to VLS synthesis, the growth rate, v , turns out to be NW diameter dependent through the supersaturation, $\Delta\mu$, as follows:

$$\Delta\mu = \Delta\mu_0 - \frac{4\Omega\alpha}{d_{\text{NW}}}, \quad (2.3)$$

where $\Delta\mu_0$ is the chemical potential difference of the Si compound in the vapor phase and solid phase in the NW at a plane boundary ($d_{\text{NW}} \rightarrow \infty$), Ω is the atomic volume of Si, and α is the specific energy of the NW surface [16, 19–22]. Hence, the random agglomeration of gold catalyst droplets results in the formation of silica NWs of different diameters growing with different velocities.

- *Nanospring formation* - The formation of silica NSs is attributed to the diffusion of gold/silicon catalyst droplets while NWs grow. Migration/diffusion of gold during VLS NW growth has been previously reported [17, 23–25] for the silicon NWs synthesized at the reaction chamber pressure ≤ 0.3 Torr (down to ultrahigh vacuum [23]) and at temperatures $\geq 450^\circ\text{C}$. Under these growth conditions, the gold migration

from the catalyst droplet onto the NW sidewalls, the conical forms and termination of growth of silicon NWs have been observed. In our case of the relatively high (atmospheric) pressure and low growth temperature (350°C), gold/silicon catalyst droplets can partially diffuse to form a nonuniform asymmetric liquid alloy structure as shown in Figs. 2.1 (c) and 2.1 (d). The difference in the growth rates of the silica NWs and the nonuniform asymmetrical properties of the liquid gold/silicon alloy catalyst result in the formation of the surface tension forces and corresponding torque, that twists the growing system around its center of mass, as schematically demonstrated in Figs. 2.1 (c) and 2.1 (d). Silica NSs consist of multiple silica NWs coherently twisted by the surface tension forces during VLS growth to form the structures illustrated in Figs. 2.1 (e) and 2.2 (a). The average growth rate of silica NSs is $\sim 2.5 \mu\text{m}/\text{min}$, while the average silicon NWs growth rate is $\sim 0.5 \mu\text{m}/\text{min}$ [23,24]. This difference in the growth velocities of silicon NWs and silica NSs is attributed to the silicon–oxygen bonding energy in the silica structure. In terms of the supersaturation quantities corresponding to Si compound in the silica NS and silicon NW VLS processes, the following relation can be written:

$$\Delta\mu_{\text{Si}}^{(\text{SiO}_2)} = \Delta\mu_{\text{Si}}^{(\text{Si})} + \delta\mu_{\text{Si-O}}, \quad (2.4)$$

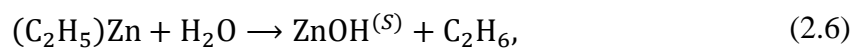
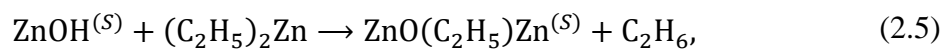
where $\Delta\mu_{\text{Si}}^{(\text{SiO}_2)}$ and $\Delta\mu_{\text{Si}}^{(\text{Si})}$ are the chemical potential differences of the Si compound in the vapor phase and solid phases in the silica NS and silicon NW, respectively; $\delta\mu_{\text{Si-O}}$ is the chemical potential quantity associated with the silicon–oxygen bonding in silica NS structure. In other words, oxidation of silicon at the NS tip–catalyst droplet

interface enhances the diffusion rate of silicon compound through the liquid phase and increases the NS growth rate.

2.2.2 Atomic Layer Deposition of ZnO

The nanosprings were coated with ZnO by atomic layer deposition (ALD) [26–31]. A SEM micrograph of the ZnO covered nanosprings is shown in Fig. 2.2 (b). A representative XRD pattern for ZnO coated nanosprings is displayed in Fig. 2.2 (c). The primary ZnO peaks are delineated with blue lines, where the peak delineated with a red line is the diffraction line of the (111) plane of gold catalyst.

ALD is a vapor-to-solid phase technique utilized for producing thin films of various materials. Based on sequential chemical reactions, ALD coating of silica nanosprings with ZnO proved to have a number of advantages over other deposition techniques (e.g. CVD [31]) and over self-assembled ZnO nanowire mat [32,33], such as low deposition temperature, the ability to precisely control coating thickness of the gas sensitive layer, the size of nanocrystals, and the ability to uniformly coat complex three-dimensional structures (like nanospring mats). A schematic of the ALD system constructed to coat silica NSs with MOSs is presented in Fig. 2.3 (a). The pneumatically actuated valves displayed in Fig. 2.3 (a) are controlled with a PLC (programmable logic controller) to generate sequential alternating pulses of chemical precursor vapors. ALD of ZnO on the silicon dioxide nanosprings was performed in a tube furnace at 175°C using deionized water (H₂O) and diethylzinc (DEZn) as oxygen and zinc sources, respectively [28,34]. The chemical formation of ZnO layer on the silica NS surface by ALD can be described by the repeating sequence of the following chemical reactions:



where the superscript (S) denotes the surface species [28,34].

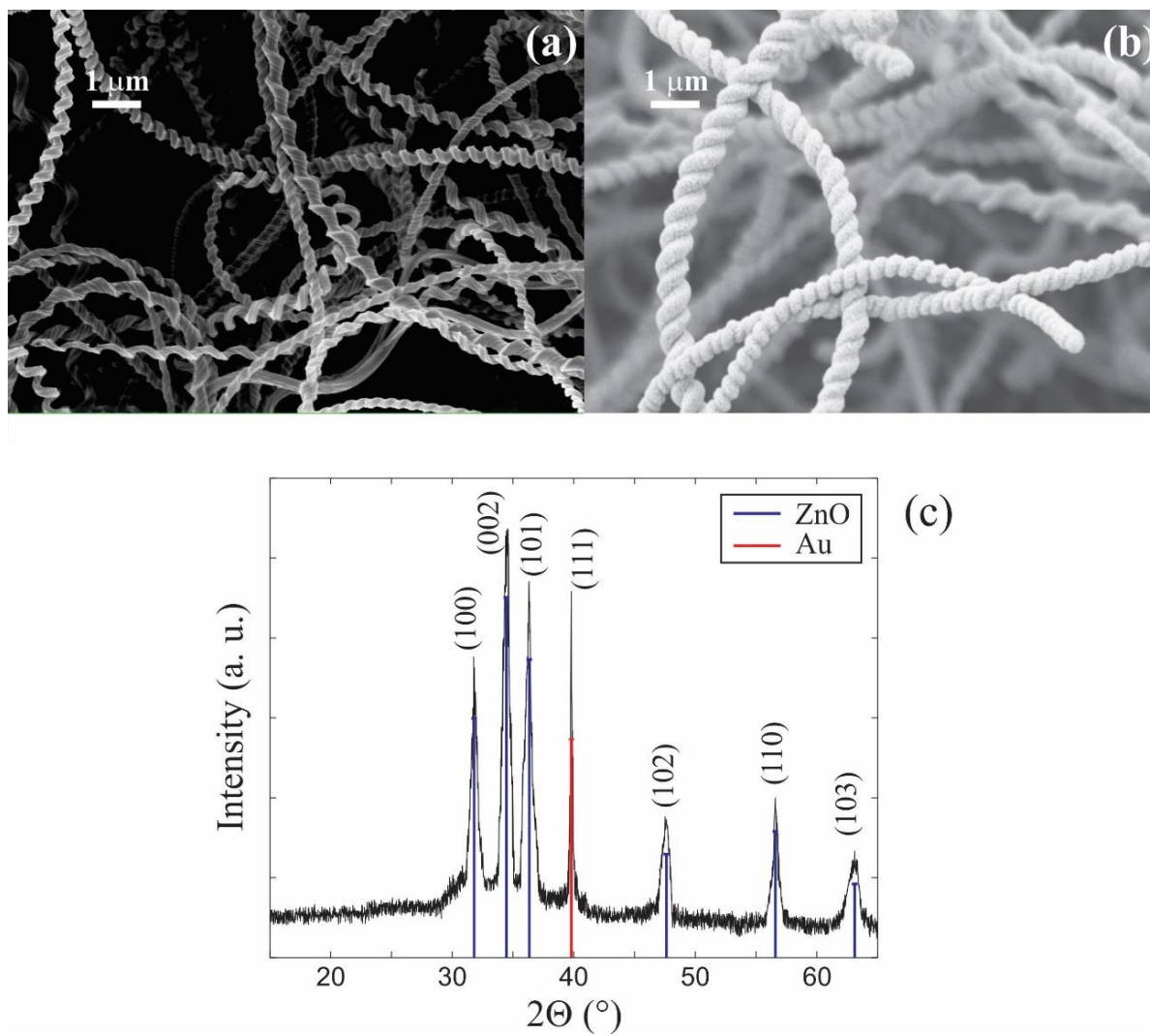


Figure 2.2 SEM micrographs of (a) a silica nanospring mat, (b) of ZnO coated nanosprings. (c) A XRD spectrum of ZnO coated nanosprings.

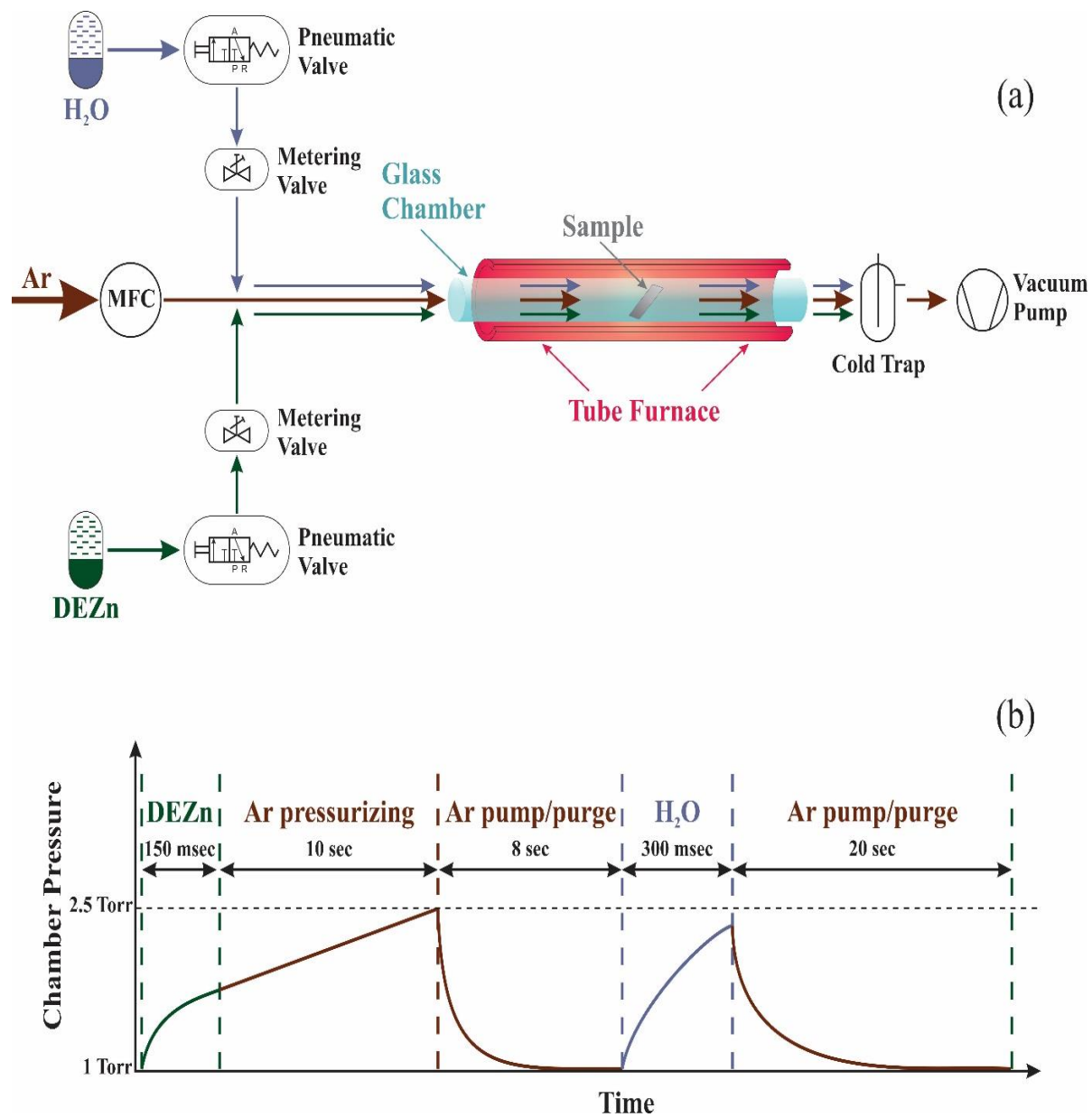
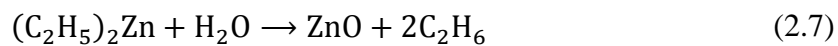


Figure 2.3 (a) Schematic of the ALD system utilized for ZnO deposition. (b) The variation of the chamber pressure during each cycle.

Thus, the ALD chemical reaction splits the CVD process



into two half-reactions (2.5) and (2.6) [34].

During the deposition, the reaction chamber was maintained at approximately 1 Torr with a constant flow rate of 6 sccm of Ar. An ALD cycle consisted of 150 msec DEZn pulse, followed by pressurization to 2.5 Torr of Ar for 10 sec, an 8 sec Ar pump/purge, a 300 msec water pulse, followed by another 20 sec Ar pump/purge. The variation of the chamber pressure during each cycle is schematically shown in Fig. 2.3 (b). A typical 50 nm ZnO coating required 100 ALD cycles.

2.3 Electrical Characterization

A schematic of the gas sensor test station is presented in Fig. 2.4 (a). A standard two-electrode test geometry was used to measure the electrical response of the xenon light bulb chemiresistor. The light bulb chemiresistor was mounted in a jig with spring loaded electrodes and a spring loaded thermocouple contacting the mat of ZnO coated silica nanosprings (see Figs. 2.4 (b) and 2.4 (c)). The xenon light bulb was powered using a variac. The resistance of the chemiresistor was measured using a Kiethley 2400 source- sense meter interfaced to a computer via Labview-operated data acquisition software for real time acquisition. The xenon light bulb sensor was placed in a tubular chamber. A continuous gas stream of synthetic air (20% O₂ and 80% N₂) into the chamber was maintained at all times. Toluene vapor was produced by bubbling Ar through a flask filled with toluene. Sequential pulses of toluene vapor were introduced into the gas stream with a solenoid valve placed downstream of the bubbler. Temperature regulation of the vapor-gas mixture (toluene vapor and synthetic air) was achieved by passing it through a heated coil of ¼" diameter stainless steel tubing. The calculated partial vapor pressure of the analyte in the ambient atmosphere was 1000 ppm.

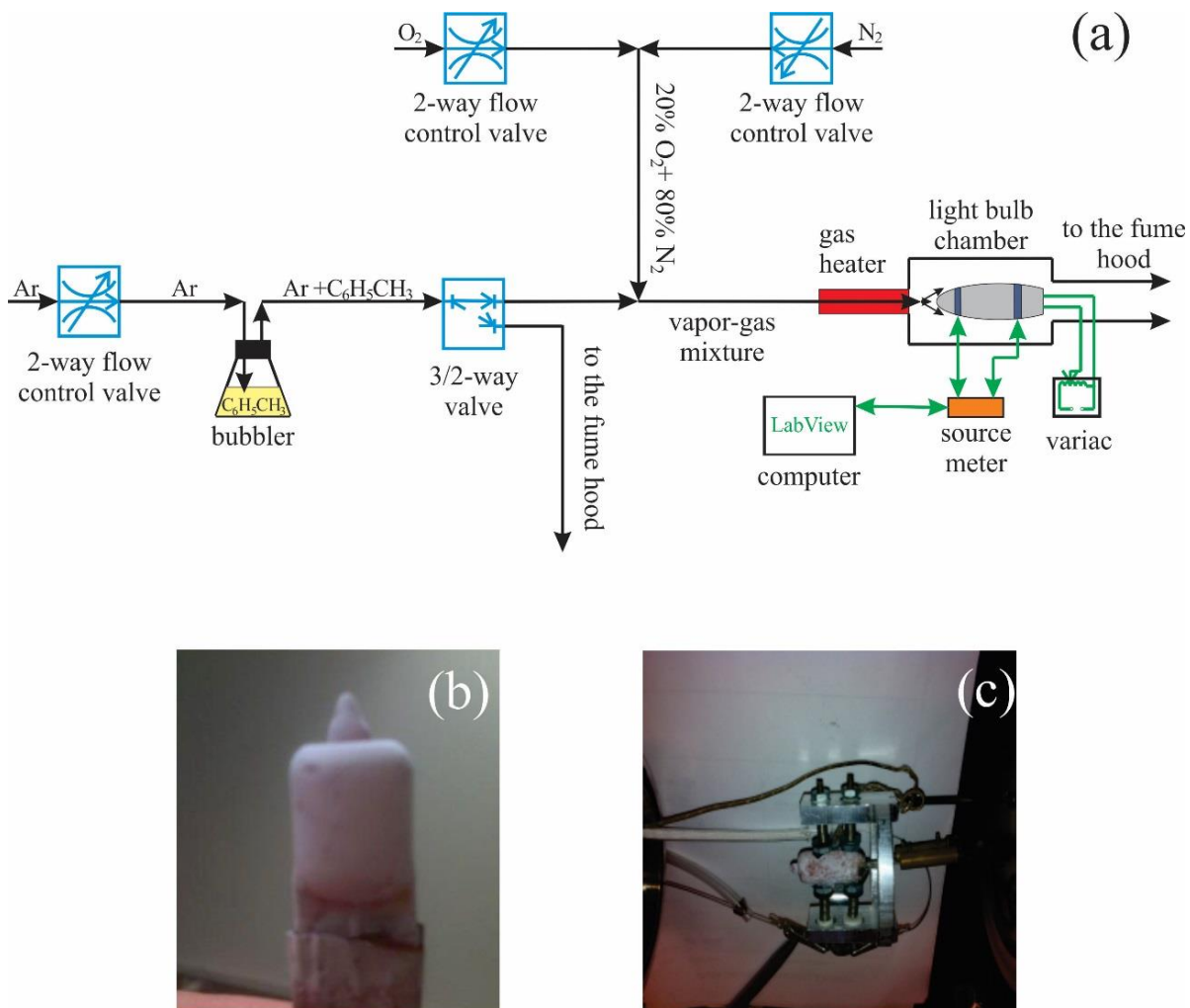


Figure 2.4 (a) A schematic of the experimental setup used to acquire electrical response of the xenon light bulb chemiresistor, (b) the xenon light bulb sensor and (c) the light bulb sensor mounted in the jig.

2.4 Results

The electrical sensor response to toluene as a function of xenon light bulb sensor surface temperature (T_{LB}) and vapor-gas mixture temperature (T_V) was studied and evaluated. The

first set of experiments was aimed at determining the electrical response of a sensor to toluene vapor as a function of the xenon light bulb sensor surface temperature (T_{LB}). The experiment was conducted without any heating of the vapor-gas mixture ($T_V = 22^\circ\text{C}$). The procedure for experimental data acquisition was to allow the sensor to reach steady state resistance in the synthetic air at a given temperature T_{LB} , at which time it was exposed to room temperature pulses of the vapor-gas mixture. Note, pulses of Ar sans toluene did not produce a significant sensor response. The results for $T_{LB} = 280^\circ\text{C}$, 370°C , and 435°C are summarized in Figs 2.5 (a), (b) and (c), respectively. The effect of temperature on the electronic properties of a thin ZnO layer deposited on the silica nanosprings is significantly different relatively to bulk ZnO. Heating bulk ZnO increases the number of carriers in the conduction band, which in its turn, leads to a drop in resistance. However, for a thin ZnO layer on silica nanosprings, where the length scale of surface interactions is comparable to the thickness of the layer, there are two competing processes. Namely, the generation of free carriers (decreasing resistance) and oxidation of the ZnO surface (increasing resistance). In the oxidation process, the adsorbed oxygen species can trap free electrons from the near-surface ZnO region (redox process) due to thermal activation [4,5]. Thermalizing of the electron carriers is needed to overcome the surface potential barrier by electron hopping and to reach the oxygen species on the ZnO surface. As a result of this process, a negative surface charge is formed, which depletes the n-type ZnO semiconductor layer.

Upon exposure to toluene vapor, the resistance changes by a factor of 3 at $T_{LB}=280^\circ\text{C}$ (Fig. 2.5 (a)), 7 at $T_{LB} = 370^\circ\text{C}$ (Fig. 2.5 (b)), and 11 at $T_{LB} = 435^\circ\text{C}$ (Fig. 2.5 (c)). Note, the xenon light bulb chemiresistor is *not* self-refreshing in the synthetic air at $T_{LB} = 280^\circ\text{C}$ (Fig. 2.5 (a)), as apparent from systematic decrease in its baseline with sequential exposures.

However, at higher temperatures ($T_{LB} \geq 370^\circ\text{C}$) it *is* self-refreshing. The optimal (maximum) sensor response to room temperature pulses of toluene is at $T_{LB}=435^\circ\text{C}$ (Fig. 2.5 (c)). For $T_{LB} > 435^\circ\text{C}$ the sensor response begins to decrease (not shown), which is attributed to surface phonon enhanced desorption of oxygen from the ZnO surface.

The second set of experiments was aimed at determining the chemiresistor response for $T_{LB} = 435^\circ\text{C}$ to toluene vapor as a function of the vapor-gas mixture temperature (T_V) (Fig. 2.6). The sensor resistance characteristics were obtained at vapor-gas mixture temperatures of 100°C , 200°C , 250°C , and 300°C , which correspond to Figs. 2.6 (a), 2.6 (b), 2.6 (c), and 2.6 (d), respectively. From examination of Fig. 2.6, it is apparent that the electrical response increases with increasing T_V until the maximum at $T_V = 250^\circ\text{C}$, at which point the response begins to decrease at subsequently higher temperatures. The maximum relative change in the sensor resistance at $T_V = 250^\circ\text{C}$ and at $T_{LB} = 435^\circ\text{C}$ is a factor of 27 (Fig. 2.6 (c)). The drop in sensor response for $T_V = 300^\circ\text{C}$ (Fig. 2.6 (d)) is due to the atmospheric oxidation of the toluene vapor prior to reaching the light bulb surface. As a consequence, the concentration of unoxidized toluene reaching the ZnO surface is significantly reduced relative to lower gas-vapor temperatures.

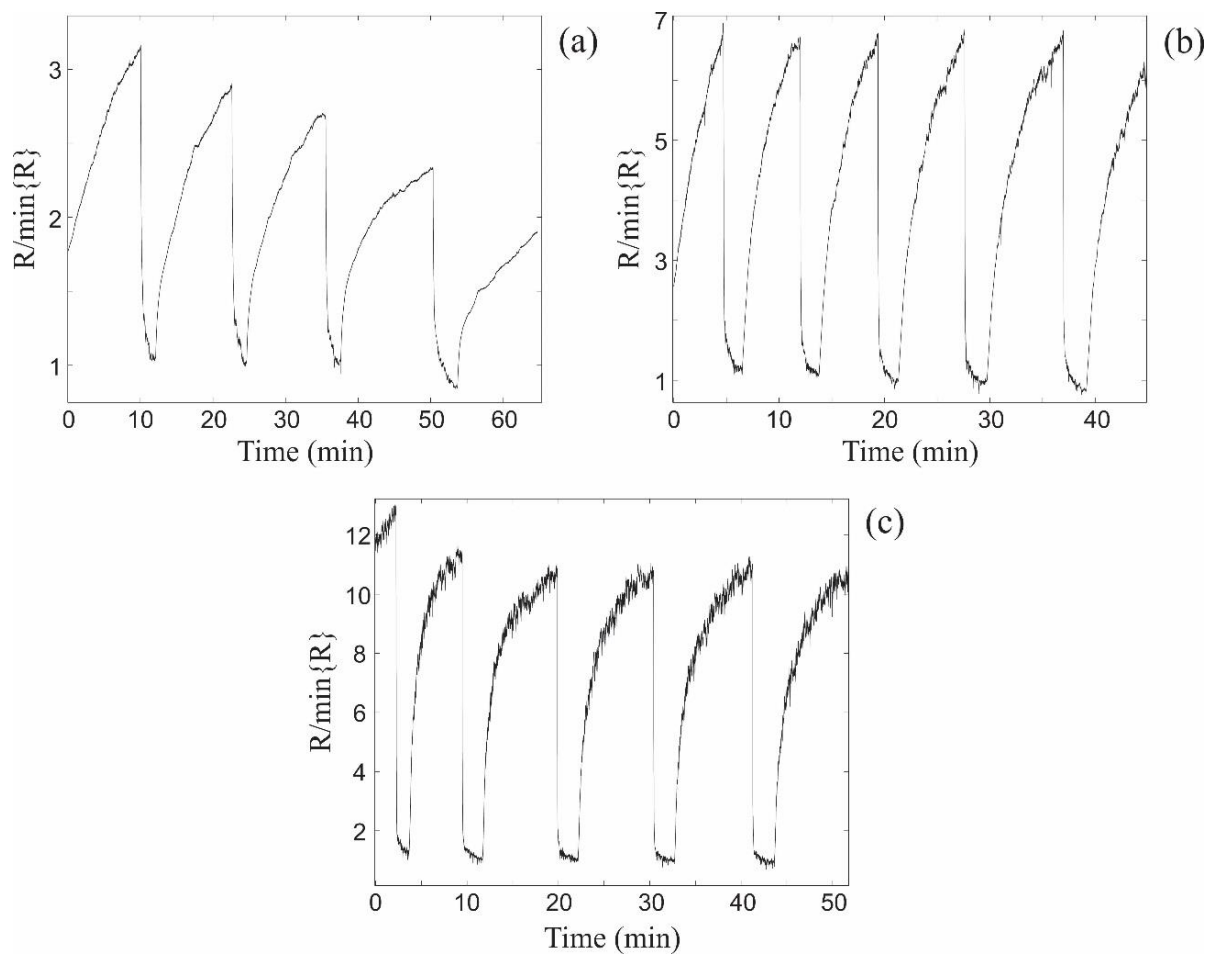


Figure 2.5 The relative changes in resistance of the light bulb ZnO nanospring sensor at (a) $T_{LB} = 280^\circ\text{C}$, (b) $T_{LB} = 370^\circ\text{C}$, and (c) $T_{LB} = 435^\circ\text{C}$ upon exposure to sequential 1000 ppm toluene pulses at fixed vapor-gas temperature $T_V = 22^\circ\text{C}$.

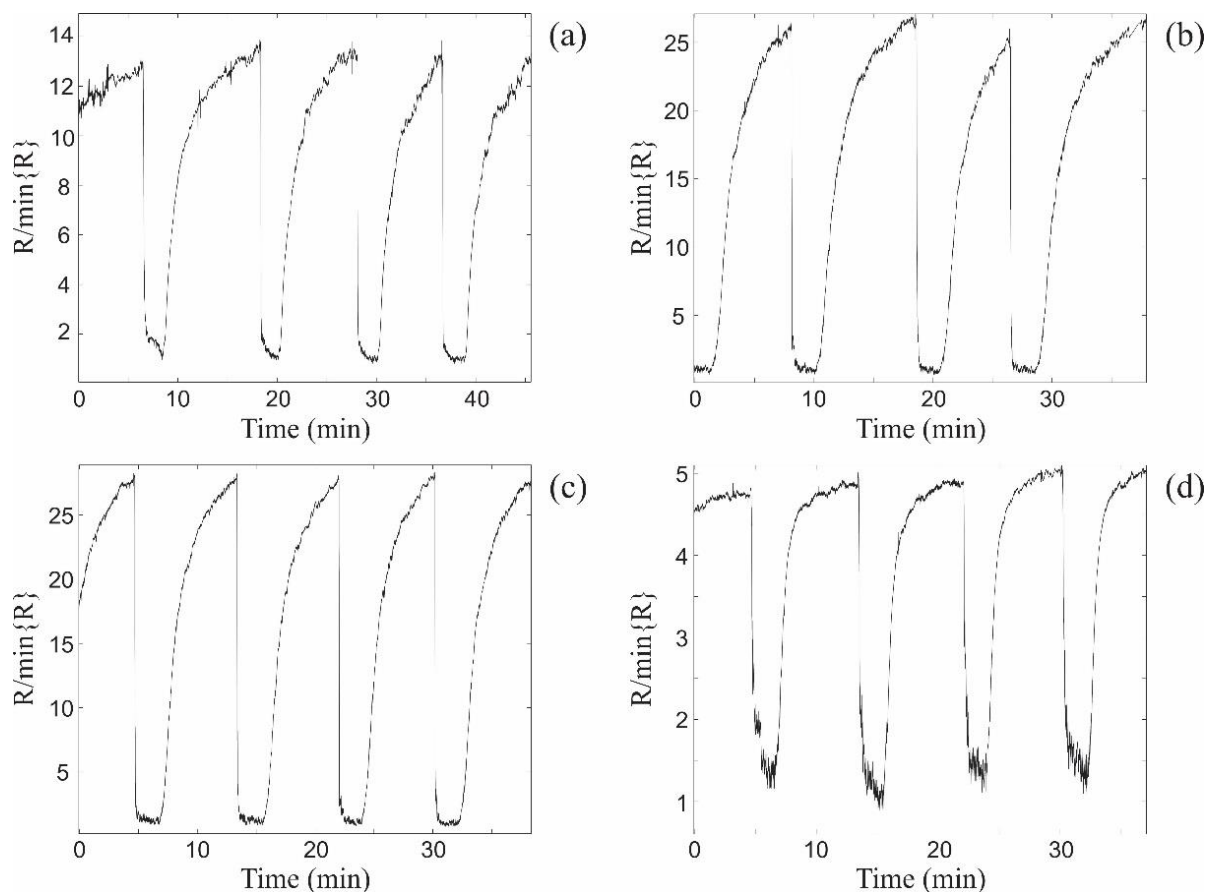


Figure 2.6 The relative changes in resistance of the xenon light bulb ZnO nanospring sensor upon exposure to 1000 ppm consequent toluene pulses at different vapor gas mixture temperatures T_V and the optimal light bulb temperature $T_{LB} = 435^\circ\text{C}$. (a) $T_V = 100^\circ\text{C}$, (b) $T_V = 200^\circ\text{C}$, (c) $T_V = 250^\circ\text{C}$, and (d) $T_V = 300^\circ\text{C}$.

2.5 Discussion

The effects of chemisorption on the electrical transport properties of metal oxides is well documented [1–11,35–38]. In the case of $\text{ZnO}_{1-\delta}$, where the surface is oxygen deficient, the surface readily oxidized in ambient air to obtain the ideal surface stoichiometry of ZnO. The oxidation process involves either chemisorption ($\text{O}_2 + e^- = \text{O}_2^-$) or dissociative

chemisorption ($O_2+2e^- = 2O^-$), where these act as traps of conduction electrons in the near-surface region of the ZnO layer. It has been reported in the literature [5,7] that below 150°C the molecular adsorption of oxygen dominates, while above 150°C dissociative chemisorption of oxygen prevails. On the other hand, at relatively high temperatures ($T > 435^\circ\text{C}$) the excitation of surface phonons leads to enhancement of oxygen desorption from the ZnO surface. The net effect is a decrease of sensor response (sensitivity) when the oxygen desorption rate exceeds the oxygen chemisorption rate.

The result of oxygen chemisorption process is the formation of a surface charge (Q_s) depleting the n-type ZnO semiconductor. The width of the depletion layer L , the Debye screening length L_D , and the height of the surface potential barrier ΔV are related by the following equation [11,37]:

$$L = L_D \left(\frac{e\Delta V}{kT} \right), \quad (2.8)$$

where e is the electron charge, k is the Boltzmann constant, and T is the absolute temperature.

The Debye screening length is given by the relationship,

$$L_D = \sqrt{\frac{\epsilon kT}{e^2 N}}, \quad (2.9)$$

where ϵ is the dielectric constant of the material and N is the carrier density. The surface barrier height ΔV is determined by the surface charge Q_s

$$\Delta V = \frac{Q_s^2}{2\epsilon\epsilon_0 N}. \quad (2.10)$$

A schematic representation of the effects of surface charge depletion on the sensor response is illustrated in Fig. 2.7. The response to toluene is attributed to the toluene oxidation at the ZnO surface and the corresponding reduction of the negative surface charge. This, in turn, decreases the depletion width producing a drop in the sensor resistance. Self-refreshing re-oxidation of the ZnO surface (redox process) returns the chemiresistor characteristics to their baselines.

In the case of heating the vapor-gas mixture at fixed sensor surface temperature $T_{LB} = 435^{\circ}\text{C}$, two processes take place on the surface. The first is simply the filling of unoccupied oxygen sites, while the second is increase of dissociative chemisorption of oxygen that results in ionic oxygen (O^-) species on the ZnO surface. On the one hand, the heating of the synthetic air enables oxygen to activate additional surface sites, thus, increasing the concentration of adsorbed oxygen species. In addition, the gas heating enhances the rate of dissociative chemisorption of oxygen, thus, increasing the concentration of ionic oxygen (O^-) species on the ZnO surface. These changes in the concentration and chemical forms of surface oxygen lead to the increment of the baseline resistance (Fig. 2.8 (a)) and an enhancement of the sensor sensitivity. On the other hand, the gas heating intensifies the toluene oxidation process in the ambient air prior to reaching the surface. This, in turn, decreases the toluene oxidation rate at the ZnO surface, thereby reducing the sensitivity. The cumulative effect of the three processes on the chemiresistor response is illustrated by Fig. 2.8 (b). Namely, the graph demonstrates that the sensor response grows until the temperature of flowing gases reaches 200°C . Between $200^{\circ}\text{C} - 250^{\circ}\text{C}$ the aforementioned effects counterbalance one another such that the sensor response plateaus. Above 250°C , the pre-oxidation of toluene in the synthetic air prevails, leading to a decline in sensitivity of the sensor. More simply stated, the activation of additional

oxygen sites at the ZnO surface enhances the oxidation rate of the analyte, but this is countered by gas phase oxidation of analyte, thereby reducing the number of unoxidized species impinging on the ZnO surface.

The self-refreshing re-oxidation (redox process) of the ZnO surface and toluene surface oxidation processes can be described with relatively high precision by the exponential functions ρ_{\uparrow} and ρ_{\downarrow} , respectively.

$$\rho_{\uparrow} = \rho_0 \left(1 - \exp \left\{ -\frac{t}{\tau_{\uparrow}} \right\} \right), \quad t < t_0; \quad (2.11)$$

$$\rho_{\downarrow} = \rho_0 \left(1 - \exp \left\{ -\frac{t_0}{\tau_{\uparrow}} \right\} \right) \exp \left\{ \frac{(t_0 - t)}{\tau_{\downarrow}} \right\}, \quad t > t_0; \quad (2.12)$$

where ρ_0 is the pre-exponential factor, t_0 is the starting time for the introduction of toluene vapor into the flow of the synthetic air, and τ_{\uparrow} and τ_{\downarrow} are the characteristic recovery and response time constants, respectively, which can be determined graphically from the data as shown in Fig. 5 (a). The time constants τ_{\uparrow} and τ_{\downarrow} are inversely proportional to the oxygen adsorption rate R_a and the toluene oxidation rate R_d on the ZnO surface, respectively.

$$\tau_{\uparrow} \propto R_a^{-1}, \quad \tau_{\downarrow} \propto R_d^{-1}. \quad (2.13)$$

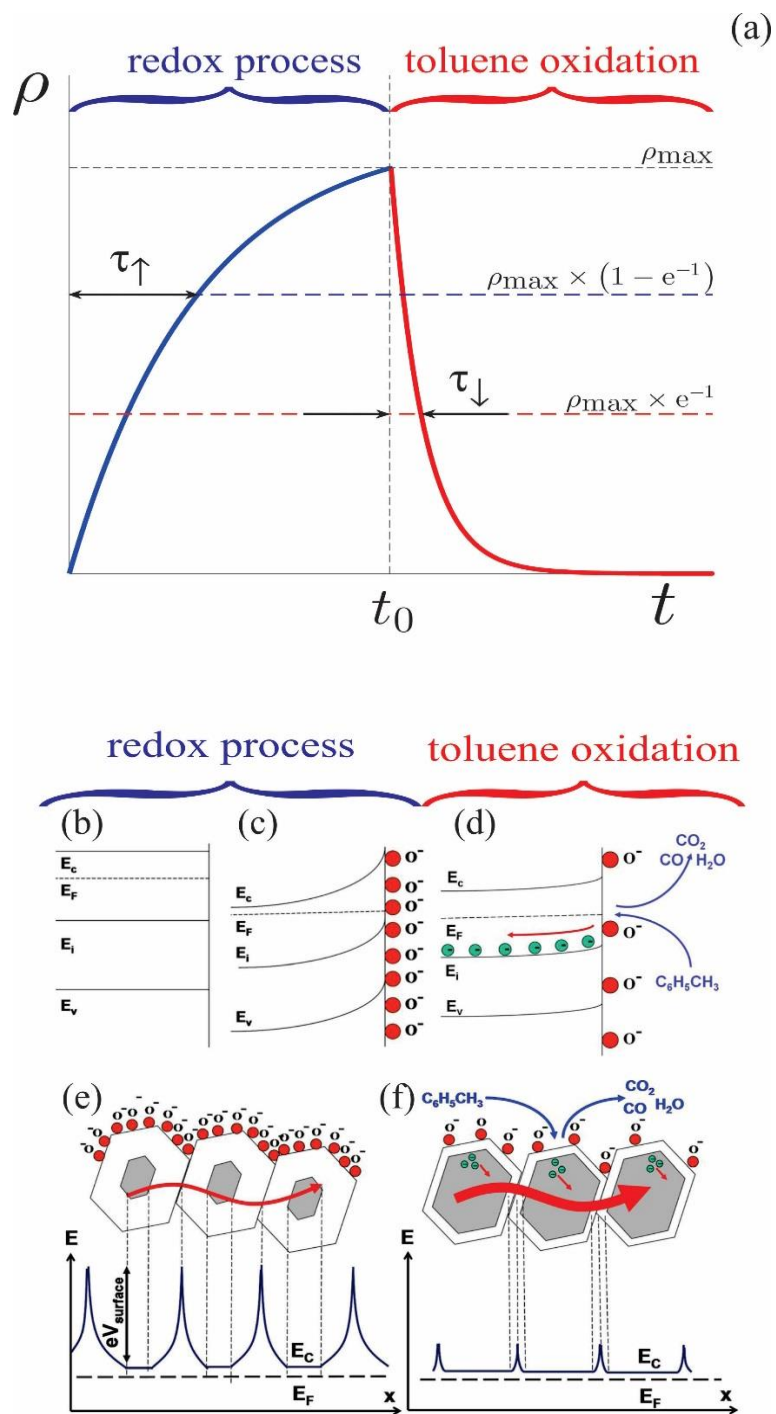


Figure 2.7 (a) Exponential ‘RC-circuit’ approximation of the sensor response. Energy level schematics (b) of the bulk ZnO, (c) at the depleted surface of ZnO, and (d) upon toluene oxidation on the ZnO surface (arbitrary intrinsic E_i levels

correspond to defect states in n-type ZnO). Schematic energy-level diagrams of the polycrystalline ZnO layer (e) prior to toluene exposure and (f) after exposure and subsequent toluene oxidation [1–3].

The rate of the oxygen adsorption on the ZnO surface, R_a , can be expressed in the same way as any kinetic process, i.e. as a product of the incident flux F of O_2 molecules and the sticking coefficient, or sticking probability, s :

$$R_a = F \cdot s. \quad (2.14)$$

The molecular flux, F , is given by the Hertz-Knudsen equation,

$$F = \frac{P}{(2\pi mkT_{GS})^{1/2}}, \quad (2.15)$$

where P is the gas pressure, m is the mass of one oxygen molecule, T_{GS} is the absolute gas temperature near the surface, which is usually taken as equal to the absolute surface temperature (T_{LB}). The sticking coefficient s is usually expressed in an Arrhenius form [35]

$$s = A \exp\left\{-\frac{E_a}{RT_{LB}}\right\}, \quad (2.16)$$

where A is the pre-exponential factor, E_a is the activation energy of oxygen adsorption on the ZnO surface, and R is the universal gas constant. Hence, the oxygen adsorption rate R_a can be written as

$$R_a = A \frac{P}{(2\pi mkT_{GS})^{1/2}} \exp\left\{-\frac{E_a}{RT_{LB}}\right\}. \quad (2.17)$$

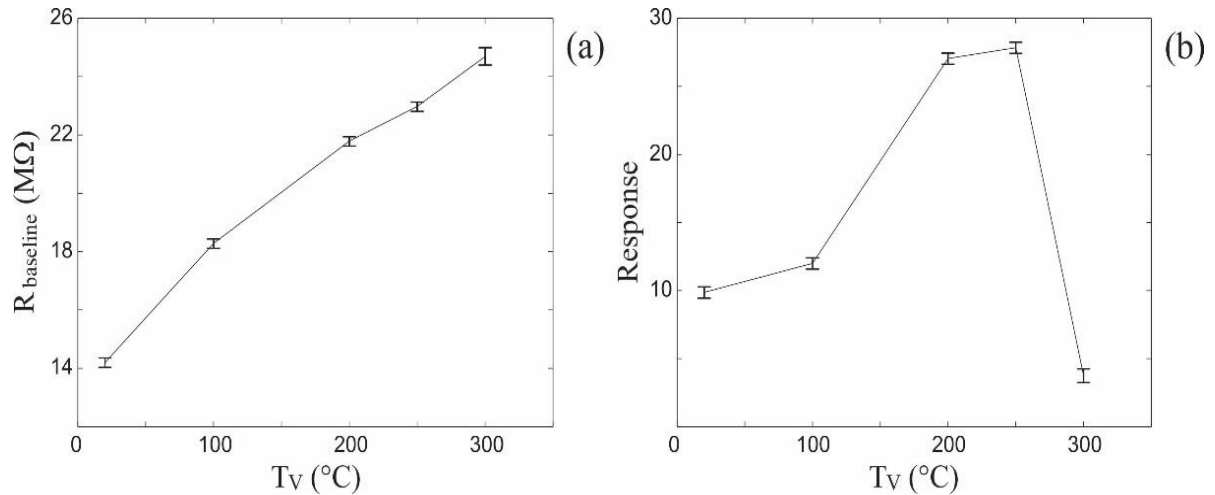


Figure 2.8 (a) The average baseline resistance of the xenon light bulb ZnO nanospring sensor ($T_{LB}=435^{\circ}C$) at different vapor gas mixture temperatures T_V . (b) The average change in the chemiresistor response to 1000 ppm toluene vapor at different vapor gas mixture temperatures T_V ($T_{LB}=435^{\circ}C$).

The catalytic surface oxidation of toluene causes the corresponding desorption (depletion) of oxygen from the ZnO surface. The desorption rate R_d of an adsorbate from the surface can be described in an Arrhenius form [36],

$$R_a = D \exp \left\{ -\frac{E_d}{RT_{LB}} \right\}, \quad (2.18)$$

where D is the pre-exponential factor and E_d is the activation energy of oxygen desorption due to the catalytic oxidation of toluene vapor on the ZnO surface.

From relation (2.13) and equations (2.17), and (2.18) the activation energies E_a and E_d can be expressed in terms of the characteristic time constants and temperature T_{LB} of the xenon light bulb chemiresistor as follows:

$$E_a = R \frac{T_{LB}^{(1)} T_{LB}^{(2)}}{T_{LB}^{(2)} - T_{LB}^{(1)}} \ln \left\{ \frac{\tau_{\uparrow}(T_{LB}^{(1)}) \sqrt{T_{LB}^{(2)}}}{\tau_{\uparrow}(T_{LB}^{(2)}) \sqrt{T_{LB}^{(1)}}} \right\}, \quad (2.19)$$

$$E_d = R \frac{T_{LB}^{(1)} T_{LB}^{(2)}}{T_{LB}^{(2)} - T_{LB}^{(1)}} \ln \left\{ \frac{\tau_{\uparrow}(T_{LB}^{(1)})}{\tau_{\uparrow}(T_{LB}^{(2)})} \right\}. \quad (2.20)$$

In equations (2.19) and (2.20) the superscripts ⁽¹⁾ and ⁽²⁾ refer to the different absolute sensor temperatures T_{LB} . The average values of the activation energies E_a and E_d , based on the above analysis, have been determined to be 83 kJ/mol and 87 kJ/mol, respectively.

The graphically determined values of characteristic recovery (τ_{\uparrow}) and response (τ_{\downarrow}) time constants as functions of temperatures T_{LB} and T_V from Figures 3 and 4 are summarized in Table 2.1. The decrease of both the time constants with increasing xenon light bulb temperature (T_{LB}) at a fixed vapor temperature of $T_V = 22^{\circ}\text{C}$ is in good agreement with Arrhenius relationships in Eqs. (2.17) and (2.18) for the oxygen adsorption and desorption rates, respectively. The characteristic response time τ_{\downarrow} remains constant for $22^{\circ}\text{C} < T_V < 250^{\circ}\text{C}$, while the increase of the characteristic recovery time τ_{\uparrow} with increasing T_V from 22°C to 250°C (at the fixed sensor temperature $T_{LB} = 435^{\circ}\text{C}$) also correlates with Eq (2.17), under the assumption that the gas temperature T_{GS} (see Eq. (2.17)) near the ZnO surface rises with the increment of T_V . Heating the vapor-gas mixture reduces the interaction time between oxygen molecules and the ZnO surface and, hence, decreases the oxygen adsorption rate on the ZnO surface. The significant rise of both the time constants τ_{\uparrow} and τ_{\downarrow} at $T_{LB} = 435^{\circ}\text{C}$ and $T_V = 300^{\circ}\text{C}$ is attributed to the increase in the gas phase oxidation rate of toluene prior to reaching the ZnO surface.

Table 2.1 Characteristic recovery (τ_{\uparrow}) and response (τ_{\downarrow}) time constants at different xenon light bulb temperatures (T_{LB}) and vapor gas mixture temperatures (T_V).

	$T_{LB}=280^{\circ}\text{C}$ $T_V=22^{\circ}\text{C}$	$T_{LB}=370^{\circ}\text{C}$ $T_V=22^{\circ}\text{C}$	$T_{LB}=435^{\circ}\text{C}$ $T_V=22^{\circ}\text{C}$	$T_{LB}=435^{\circ}\text{C}$ $T_V=100^{\circ}\text{C}$	$T_{LB}=435^{\circ}\text{C}$ $T_V=200^{\circ}\text{C}$	$T_{LB}=435^{\circ}\text{C}$ $T_V=250^{\circ}\text{C}$	$T_{LB}=435^{\circ}\text{C}$ $T_V=300^{\circ}\text{C}$
τ_{\uparrow} (secs)	540	42.2	11.3	12	16	18	73
τ_{\downarrow} (secs)	80	3	1.2	1.2	1.2	1.2	10

2.6 Conclusions

A new approach to fabricating an ultra-high surface area gas sensor (chemiresistor) has been demonstrated. The chemiresistor was constructed directly onto the surface of a conventional xenon light bulb (used as a sensor heater) by coating it with a 3-D ZnO coated silica nanospring mat. The sensor response to the analyte (toluene vapor) is attributed to its oxidation at the ZnO surface, thereby creating an oxygen deficient surface of ZnO, and self-refreshing to chemisorption of atmospheric oxygen (redox process). The activation energy of ZnO surface oxidation and the activation energy of toluene oxidation on the ZnO surface were determined to be $83 \text{ kJ}\cdot\text{mol}^{-1}$ and $87 \text{ kJ}\cdot\text{mol}^{-1}$, respectively. It was shown that the relative chemiresistor response is not only highly dependent on the temperature of the ZnO surface, but also on the temperature of the vapor-gas mixture. This can be explained by the fact that both the temperatures influence the density and chemical forms (molecular or ionic) of oxygen species on the ZnO surface and the gas phase toluene oxidation rate in the ambient atmosphere. The maximum sensitivity was achieved at the xenon light bulb temperature of

435°C and at the vapor-gas mixture temperature of 250°C, but at the expense of the sensor recovery time τ_{\uparrow} , which is optimal at a vapor-gas temperature of room temperature (22°C).

References

- [1] Dobrokhotov, V.; Oakes, L.; Sowell, D.; Larin, A.; Hall, J.; Barzilov, A.; Kengne, A.; Bakharev, P.; Corti, G.; Cantrell, T.; Prakash, T.; Williams, J.; Bergman, L.; Husso, J.; McIlroy, D. Thermal and optical activation mechanisms of nanospring-based chemiresistors. *Sensors*, *12*, 5608–5622 (2012).
- [2] Dobrokhotov, V.; Oakes, L.; Sowell, D.; Larin, A.; Hall, J.; Kengne, A.; Bakharev, P.; Corti, G.; Cantrell, T.; Prakash, T.; Williams, J.; McIlroy, D. Toward the nanospring-based artificial olfactory system for trace-detection of flammable and explosive vapors. *Sensors and Actuators B: Chemical*, *168*, 138–148 (2012).
- [3] Dobrokhotov, V.; Oakes, L.; Sowell, D.; Larin, A.; Hall, J.; Kengne, A.; Bakharev, P.; Corti, G.; Cantrell, T.; Prakash, T.; Williams, J.; McIlroy, D. ZnO coated nanospring-based chemiresistor. *J. Appl. Phys.*, *111*, 044311:1–044311:8 (2012).
- [4] Bochenkov, V.; Sergeev, G. Sensitivity, selectivity, and stability of gas-sensitive metal-oxide nanostructures. In *Metal Oxide Nanostructures and Their Applications*, 2nd ed.; Umar, Hahn, Eds.; Stevenson Ranch, Calif: American Scientific Publishers; Volume 3, pp. 31–52 (2010).
- [5] Barsan, N.; Weimar, U. Conduction model of metal oxide gas sensors. *J. Electroceramics*, *7*, 143–167 (2001).

- [6] Barsan, N.; Weimar, U. Understanding the fundamental principles of metal oxide based gas sensors; the example of CO sensing with SnO₂ sensors in the presence of humidity. *J. Phys. Condens. Matter*, *15*, R813–R839 (2003).
- [7] Gurlo, A.; Bârsan, N.; Oprea, A.; Sahm, M.; Sahm, T.; Weimar, U. An n- to p-type conductivity transition induced by oxygen adsorption on α -Fe₂O₃. *Appl. Phys. Lett.*, *85*, doi:10.1063/1.1794853 (2004).
- [8] Ra, H.W.; Khan, R.; Kim, J.T.; Kang, B.R.; Im, Y.H. The effect of grain boundaries inside the individual ZnO nanowires in gas sensing. *Nanotechnology*, *21*, doi:10.1088/0957-4484/21/8/085502 (2000).
- [9] Li, Q.H.; Gao, T.; Wang, Y.G.; Wang, T.H. Adsorption and desorption of oxygen probed from ZnO nanowire films by photocurrent measurements. *Appl. Phys. Lett.*, *86*, 123117:1–123117:3 (2005).
- [10] Gas'kov, A.M.; Rumyantseva, M.N. Nature of gas sensitivity in nanocrystalline metal oxides. *J. Appl. Chem.*, *74*, 440–444 (2001).
- [11] Gas'kov, A.M.; Rumyantseva, M.N. Materials for solid-state gas sensors. *Inorg. Mater.*, *36*, 293–301 (2000).
- [12] McIlroy, D.N.; Alkhateeb, A.; Zhang, D.; Aston, D.E.; Marcy, A.C.; Norton, M.G. Nanospring formation—Unexpected catalyst mediated growth. *J. Phys. Condens. Matter*, *16*, R415–R440 (2004).
- [13] Hu, J.; Odom, T.; Lieber, C. Chemistry and physics in one dimension: synthesis and properties of nanowires and nanotubes. *Acc. Chem. Res.*, *32*(5), pp. 435–445 (1999).
- [14] Huang, M.; Wu, Y.; Feick, H.; Tran, N.; Weber, E.; Yang, P. Catalytic growth of zinc oxide nanowires by vapor transport. *Adv. Mater.*, *13*(2), pp. 113–116 (2001).

- [15] Tuan, P.; Dai, N.; Khang, D.; An, D. Some results of the nanowires growth on gallium arsenic substrates by VLS method: some theoretical aspects of the growth mechanisms and abnormal phenomena. *Proc. Natl. Conf. Theor. Phys.*, 36, pp. 228–233 (2011).
- [16] Biswas, S.; O'Regan, C.; Petkov, N.; Morris, M.; Holmes, J. Manipulating the growth kinetics of Vapor-Liquid-Solid propagated Ge nanowires. *Nano Lett.*, 13, 4044–4052 (2013).
- [17] Givargizov, E.I. Fundamental aspects of VLS growth. *Journal of Crystal Growth*, Vol. 31, pp. 20–30 (1975).
- [18] Givargizov, E. I. *Highly Anisotropic Crystals*, Springer: New York, Chapter 2 (1987).
- [19] Weyher, J. Some notes on growth kinetics and morphology of VLS silicon-crystals grown with platinum and gold as liquid-forming agents. *J. Cryst. Growth*, 43, pp. 235–244 (1978).
- [20] Wu, Y. Y.; Fan, R.; Yang, P. D. Block-by-block growth of single-crystalline Si/SiGe superlattice nanowires. *Nano Lett.*, 2, pp. 83–86 (2002).
- [21] Kikkawa, J.; Ohno, Y.; Takeda, S. Growth rate of silicon nanowires. *Appl. Phys. Lett.* 86, 123109 (2005).
- [22] Dhalluin, F.; Baron, T.; Ferret, P.; Salem, B.; Gentile, P.; Harmand J.-C. Silicon nanowires: Diameter dependence of growth rate and delay in growth. *Appl. Phys. Lett.*, 96, 133109 (2010).
- [23] Hannon, J.; Kodambaka, S.; Ross, F.; Tromp, R. The influence of the surface migration of gold on the growth of silicon nanowires. *Nature*, Vol. 440, pp. 69–71; doi:10.1038/nature04574 (2006).

- [24] Kawashima, T.; Mizutani, T.; Nakagawa, T.; Torii, H.; Saitoh, T.; Komori, K.; Fujii M. Control of surface migration of gold particles on Si nanowires. *Nano Lett.*, 8(1), pp. 362–368 (2008).
- [25] Bailly, A.; *et al.* Direct quantification of gold along a single Si nanowire. *Nano Lett.*, 8(11), pp. 3709–3714 (2008).
- [26] Johnson, R.; Hultqvist, A.; Bent, S. A brief review of atomic layer deposition: from fundamentals to applications. *Materials Today*, Vol. 17, 5, pp. 236–246 (2014).
- [27] George, S.M.; Ott, A.W.; Klaus, J.W. Surface chemistry for atomic layer growth. *J. Phys. Chem.*, 100, pp. 13121–13131 (1996).
- [28] Elam, J.W.; George, S.M. Growth of ZnO/Al₂O₃ alloy films using atomic layer deposition techniques. *Chem. Mater.*, 15, 1020–1028 (2003).
- [29] Przeździecka, E. Characterization of ZnO films grown at low temperature. *Acta Phys. Pol. A*, 114, pp. 1303–1310 (2008).
- [30] Guziewicz, E. ZnO by ALD-advantages of the material grown at low temperature. *Acta Phys. Pol. A*, 116, pp. 814–817 (2009).
- [31] Ritala, M.; Niinistö, J. Atomic layer deposition. In *Chemical Vapour Deposition: Precursors, Processes and Applications*; Jones, A.C. and Hitchman, M.L. Eds.; Royal Society of Chemistry, pp. 158–206 (2009).
- [32] Ra, H.W.; Khan, R.; Kim, J.T.; Kang, B.R.; Im, Y.H. The effect of grain boundaries inside the individual ZnO nanowires in gas sensing. *Nanotechnology*, 21, doi:10.1088/0957-4484/21/8/085502 (2010).

- [33] Li, Q.H.; Gao, T.; Wang, Y.G.; Wang, T.H. Adsorption and desorption of oxygen probed from ZnO nanowire films by photocurrent measurements. *Appl. Phys. Lett.*, 86, 123117:1–123117:3 (2005).
- [34] Ott, A.W.; Chang, R.P.H. Atomic layer-controlled growth of transparent conducting ZnO on plastic substrates. *Mater. Chem. Phys.*, 58, pp. 132–138 (1999).
- [35] Lagowski, J.; Sproles, E.; Gatos, H. Quantitative study of the charge transfer in chemisorption; oxygen chemisorption on ZnO. *J. Appl. Phys.*, 48, doi: 10.1063/1.324156 (1977).
- [36] Watanabe, H.; Wada, M.; Takahashi, T. The activation energy for oxygen desorption from zinc oxide surfaces. *Jpn. J. Appl. Phys.*, 4, 945-947, doi: 10.1143/JJAP.4.945 (1965).
- [37] Moseley, P.; Crocker, A. *Sensor materials*; Institute of Physics Pub: Bristol Philadelphia, USA; pp. 72–73 (1996).
- [38] Redondo, A.; Zeri, Y. Rates of desorption from solid surfaces: coverage dependence. *Surface Science*, 136, 41–58 (1984).

CHAPTER 3

Single ZnO Coated Nanospring Chemiresistor;

Influence of Chemiresistor Geometry on its Response Properties

Bakharev, P.; McIlroy, D. The effect of the periodic boundary conditions of a ZnO-coated nanospring on its surface redox-induced electrical response. *Nanotechnology*, 2014, 25, 475501.

Abstract

A redox chemical sensor (chemiresistor) was constructed with a single ZnO coated silica nanospring. The chemiresistor response to toluene vapor as a function of the sensor temperature (T_{NS}) and vapor temperature (T_V) was measured and analyzed. The maximum sensitivity of the single ZnO coated nanospring device occurred at the sensor temperature (T_{NS}) of 310°C and at the vapor temperature (T_V) of 250°C. The characteristics of the electrical response of a single ZnO coated nanospring device were compared to those of a ZnO thin film. The single ZnO nanospring sensor was less responsive to small changes in toluene concentration relative to the ZnO thin film, but has a lower ultimate detection level. A computational model to simulate an electrical response of the single nanospring sensor and the thin film indicated that the differences between their response characteristics is due to the geometry of the nanospring and corresponding periodic boundary conditions imposed by this geometry, which is absent in a thin film.

3.1 Introduction

Nanomaterials have been touted as the foundation of the next generation of sensors, in particular semiconducting metal oxide (SMO) nanomaterials [1–18]. The arguments for adopting nanomaterials over conventional thin films for sensors ranges from high surface to volume ratios, finite size effects, etc. In the case of metal oxide nanomaterials, the sensing mechanism of the sensors, typically referred to as chemiresistors, is attributed to the depletion, or repletion, of the oxygen at the metal oxide semiconductor (MOS) surface. In turn, this affects the depth of the surface depletion layer, leading to significant swings in the electrical resistance of chemiresistor. Numerous studies have demonstrated that the magnitude of the swing in electrical resistance is maximized when the characteristic penetration depth of the depletion layer is comparable to the represented size of nanostructures, of which the sensing layer is comprised [1–18]. While this explains the sensing mechanism and dictates the types of sensing one can achieve with a semiconducting metal oxide sensor (SMOS), but in terms of sensor design, it is of limited use. To understand this point, consider the following. If the sensor application does not require a large dynamic range, i.e. one wants to measure small changes in a narrow range of gas concentrations, then the resolution of the sensor in this range is the primary design parameter. Alternatively, if the application is to identify ultralow concentrations of a target compound in a background, then in terms of sensor design, achieving the lowest possible sensing limit trumps resolution. Ultimately, one would like to have high resolution and sensitivity to ultralow concentrations, but they are typically competing parameters. So, the question begs to be asked, under what design constraints is a SMO nanomaterial preferable to its corresponding SMO thin film? Answering this question is further complicated by the following. Nanomaterials have extremely high surface area

relative to their bulk counterparts, where the higher the surface area, the higher the concentration of active sites with which a target compound can interact. In the context of modifications of the depletion layer, it can be argued that a higher concentration of active sites will require a higher concentration of the target compound in order to access a sufficient number of active sites with spatial and temporal coincidence, thereby inducing a measurable response. Therein lies the paradox. How can a nanomaterials based sensor with extremely high surface area respond to ultralow concentrations of the target compound? The logical conclusion is that they won't. Yet there are numerous works that have demonstrated that sensors constructed with SMO nanomaterials are responsive to ultralow concentrations of the target compound [1–27].

We argue that this paradox can be resolved using geometric arguments, and that its resolution will lead to design criteria for SMO sensors. A SMO sensor consisting of a single ZnO coated silica nanospring has been constructed that demonstrates that the periodic boundary conditions imposed by the silica nanospring results in a lower absolute detection limit than a corresponding thin film SMO sensor. The results of this study are a prelude to a comprehensive understanding of more complex SMO sensors constructed with random arrays of 1-D nanomaterials.

3.2 Experimental section

An insulating mat of silicon dioxide nanosprings was grown via the VLS mechanism in a furnace operated at atmospheric pressure. A detailed description of the process was given in Chapter 2, Section 2.1. Subsequently, the insulating silica NSs were conformally coated with ZnO nanocrystal layer by ALD technique (see Section 2.2 of Chapter 2 for details). A

representative XRD pattern for ZnO coated nanosprings is displayed in Fig. 3.1 (a). The primary ZnO peaks are delineated with blue lines, where the peak delineated with a red line corresponds to the diffraction line of the (111) plane of Au, where Au is a catalyst used for

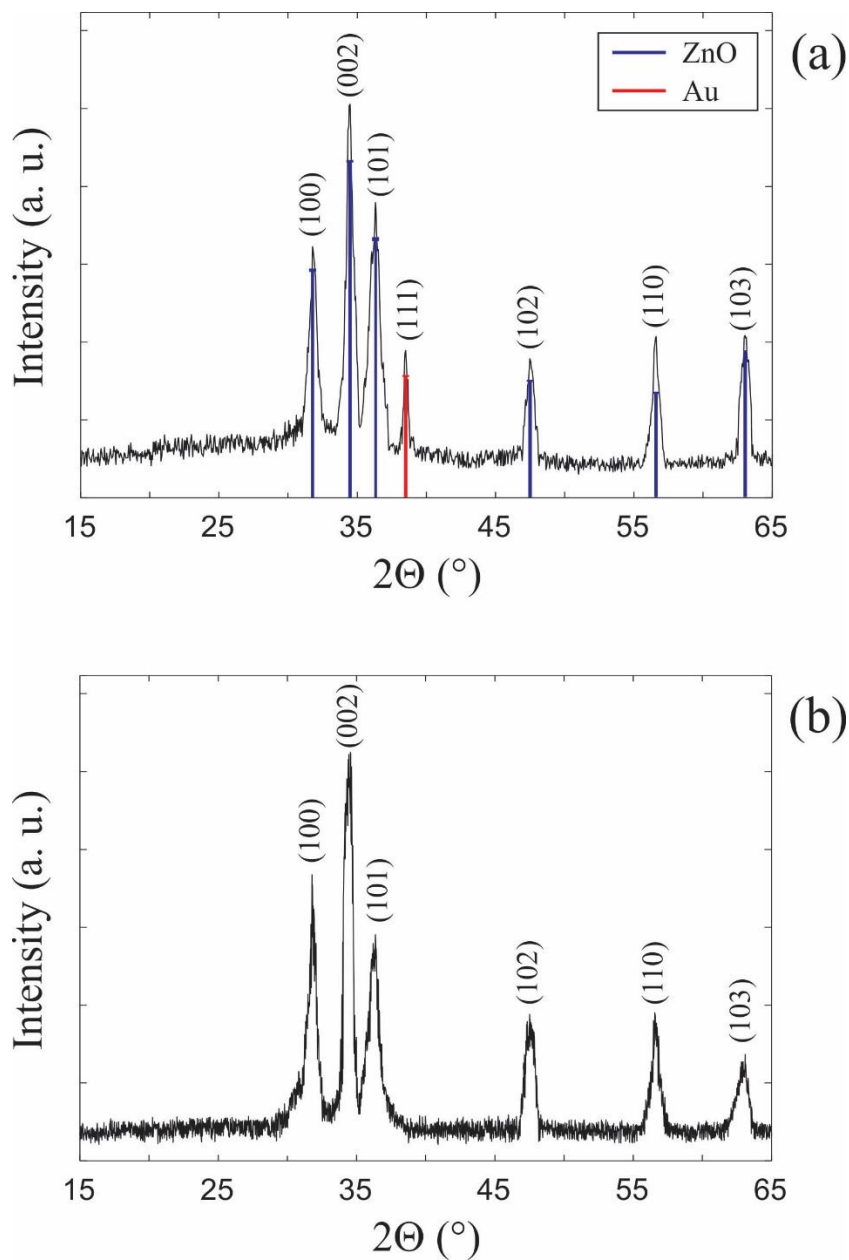


Figure 3.1 XRD spectra of (a) ZnO coated nanosprings and (b) the ZnO layer on the surface of SiO_2 wafer.

nanospring synthesis. For comparison, XRD data of a ZnO layer grown on the surface of the SiO₂ wafer is displayed in Fig 3.1 (b). The average thickness of the ZnO film measured by ellipsometry is approximately 50 nm. Figs. 3 (a) and (b) of the two XRD spectra demonstrate the equivalency of the ZnO crystal structures deposited by the same ALD processes on the substrates of different geometries.

3.2.1 ZnO coated nanospring separation

The first step in a single ZnO coated nanospring device fabrication was the separation of individual nanosprings from ZnO coated nanospring mat. That was done by transferring nanosprings from as grown ZnO coated nanospring mat sample into a beaker with isopropyl alcohol (IPA). The nanosprings suspended in IPA were separated by sonication. Then the nanospring-alcohol solution was

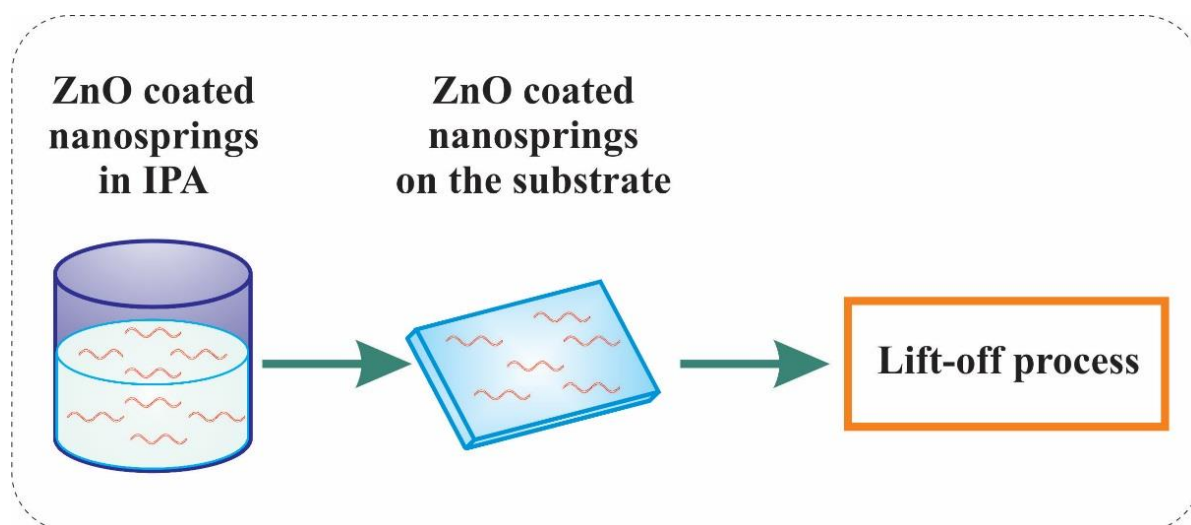


Figure 3.2 Schematics of ZnO coated nanospring separation and their transfer onto a glass substrate.

transferred onto 25 mm × 25 mm microscopic glass slides and the IPA was allowed to evaporate. The ZnO coated nanosprings separation in IPA solution and their transfer onto the glass substrate are schematically shown in Fig. 3.2. Subsequently, the electrical contacts (50 nm of Ti layer followed by 150 nm of Au layer) with a 10 μm spacing were applied to the glass substrate using standard photolithography and lift-off techniques.

3.2.2 Photolithography

Photolithography and corresponding lift-off techniques were performed in the clean room environment of class 1000. The microscopic glass surface was coated with an approximately 7 μm thick photoresist (positive resist) layer using a Laurell spin coater at 3000 – 6000 rpm for two minutes. The sample was then placed onto a hot plate for soft baking at 115°C. After baking the sample was covered with the appropriate photomask and exposed to ultraviolet (UV) light at the light dosage of 650 kJ for 30 secs using a Quintel Mask Aligner. The portion of the positive photoresist exposed to UV light becomes soluble in a tetramethyl ammonium hydroxide (TMAH) developer solution. The metallization process was performed by the successive sputtering of 50 nm thick titanium (Ti) and 150 nm thick gold (Au) layers. Titanium served as an adhesion layer for gold. The final step in the lift-off process was to remove the rest of the photoresist and any of its residues by washing the sample with acetone. A step-by-step procedure of making Ti–Au contacts by photolithography is schematically shown in Fig. 3.3.

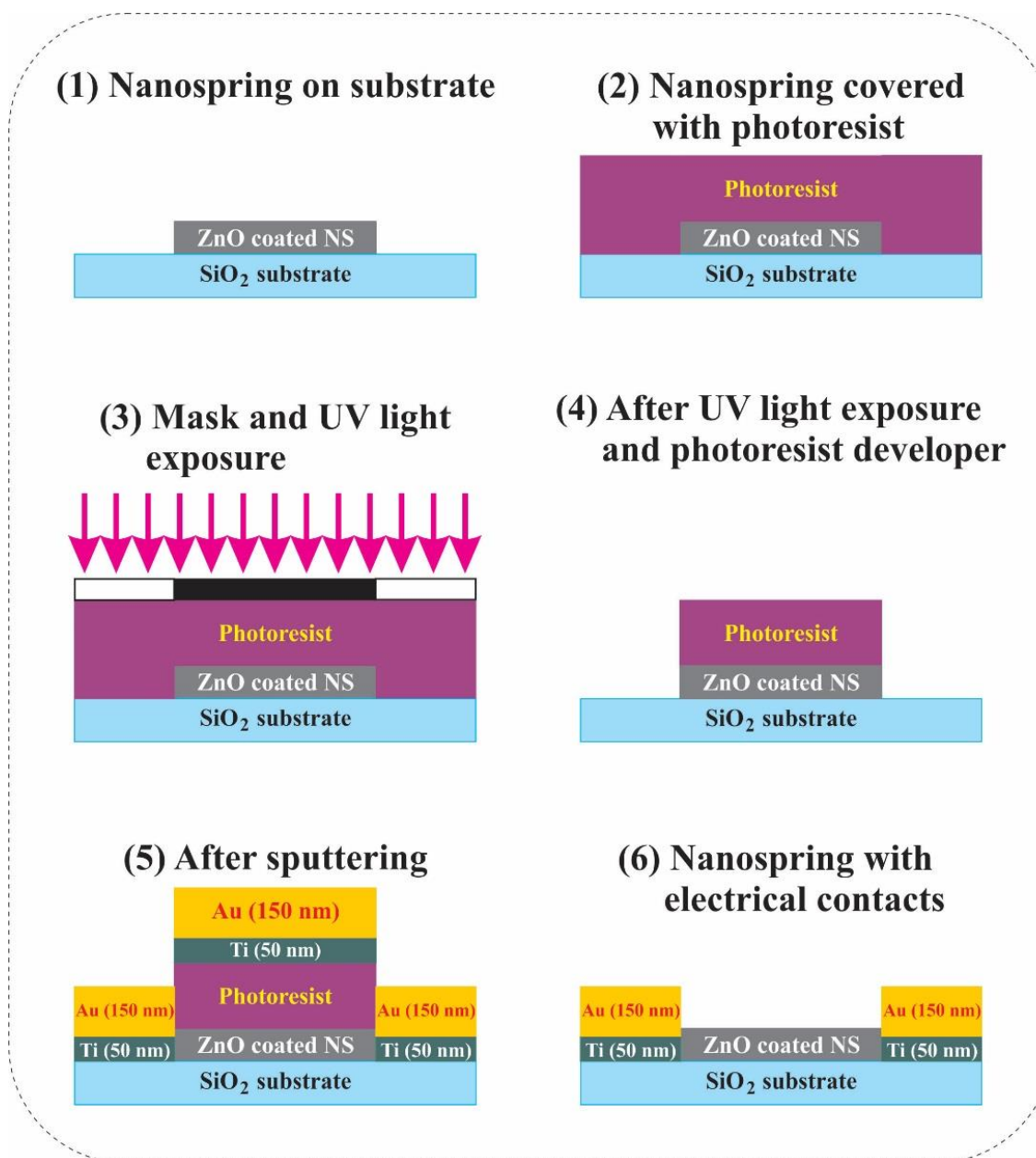


Figure 3.3 A schematic representation of a step-by-step procedure of making Ti–Au ohmic contacts by photolithography.

Prior to the electrical characterization of a single nanospring device any extra nanosprings/debris lying between ohmic Ti–Au contacts were removed under an optical microscope using micromanipulator probes to ensure that the electrical response was that of a single ZnO coated silica nanospring. SEM micrographs of individual ZnO coated

nanosprings with applied Ti–Au electrodes and schematics of a single nanospring device are illustrated in Figs. 3.4 (a) and 3.4 (b), respectively.

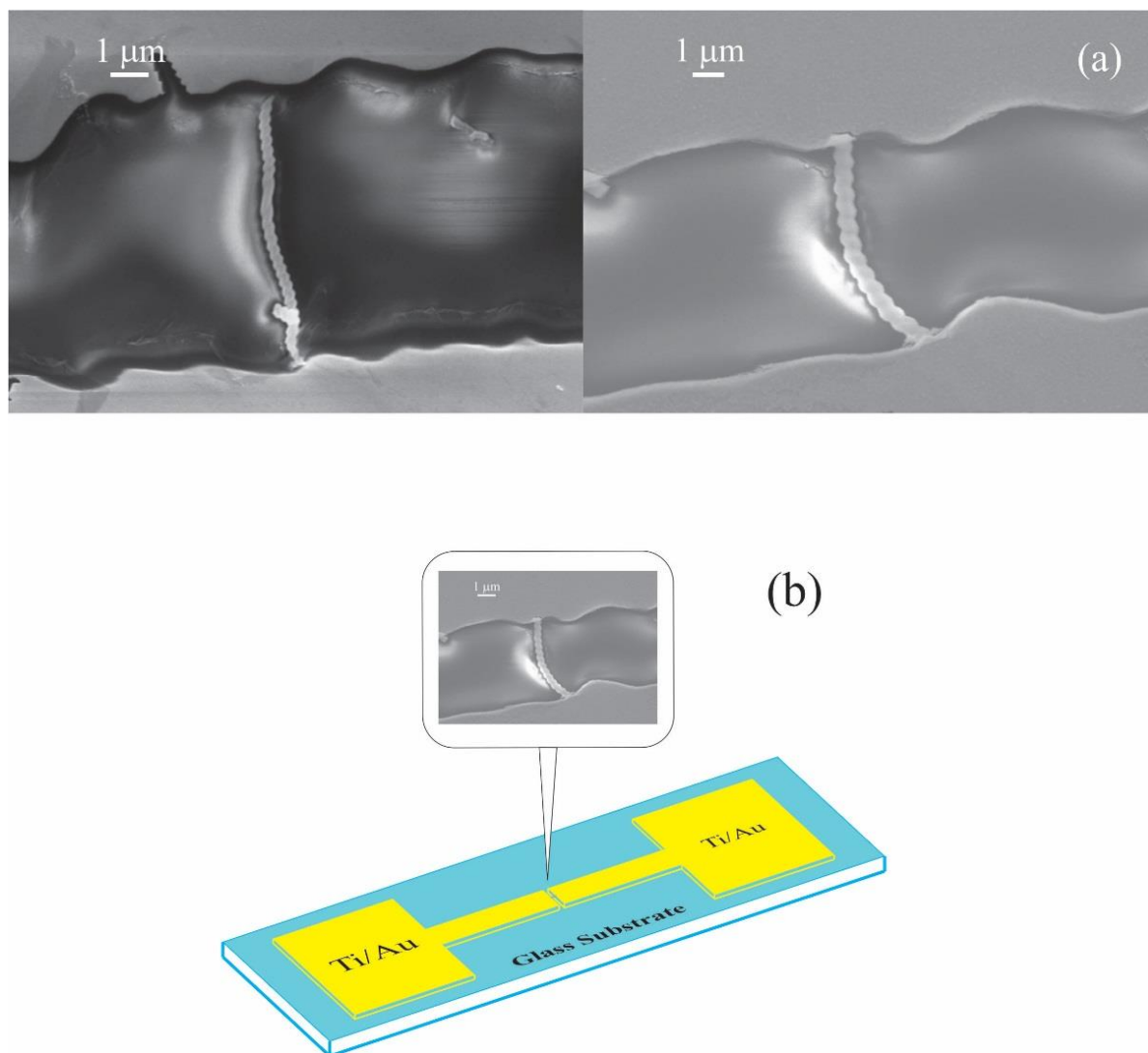


Figure 3.4 (a) individual ZnO coated nanosprings with applied Ti–Au electrodes. (b) Schematic representation of a single nanospring device.

3.2.3 Electrical Characterization

The single nanospring device was mounted to a heater to enable temperature regulation. Two electrical probes were used to make electrical contact to the Ti – Au pads. The electrical measurements were acquired using a Kiethley 2400 source-sense meter interfaced to a computer via Labview-operated data acquisition software for real time resistance measurements. The single nanospring chemiresistor was placed in a chamber through which a continuous flow of synthetic air (20% O₂ and 80% N₂) was maintained at all times. Sequential pulses of toluene vapor were generated by the constant flow of Ar gas through a bubbler of liquid toluene and a solenoid valve placed downstream of the bubbler (see Fig. 3.5 (a)). Prior to exposure to toluene vapor, the sensors were allowed to reach a steady state resistance in the synthetic air at atmospheric pressure.

The contribution of the glass substrate to the total electrical conductivity of the device was examined by comparing the I-V characteristics of the Ti–Au terminals with and without a ZnO coated nanospring present. It can be seen from the I-V curve of the open circuit at 300°C in Fig. 3.5 (b) that only a nominal current is observed, which is attributed to residual carbon on the glass surface. This current is orders of magnitude less than that of the individual ZnO coated nanospring. Moreover, unlike the single nanospring device, the electrodes devoid of a ZnO coated nanospring did not respond to the analyte (toluene) vapor.

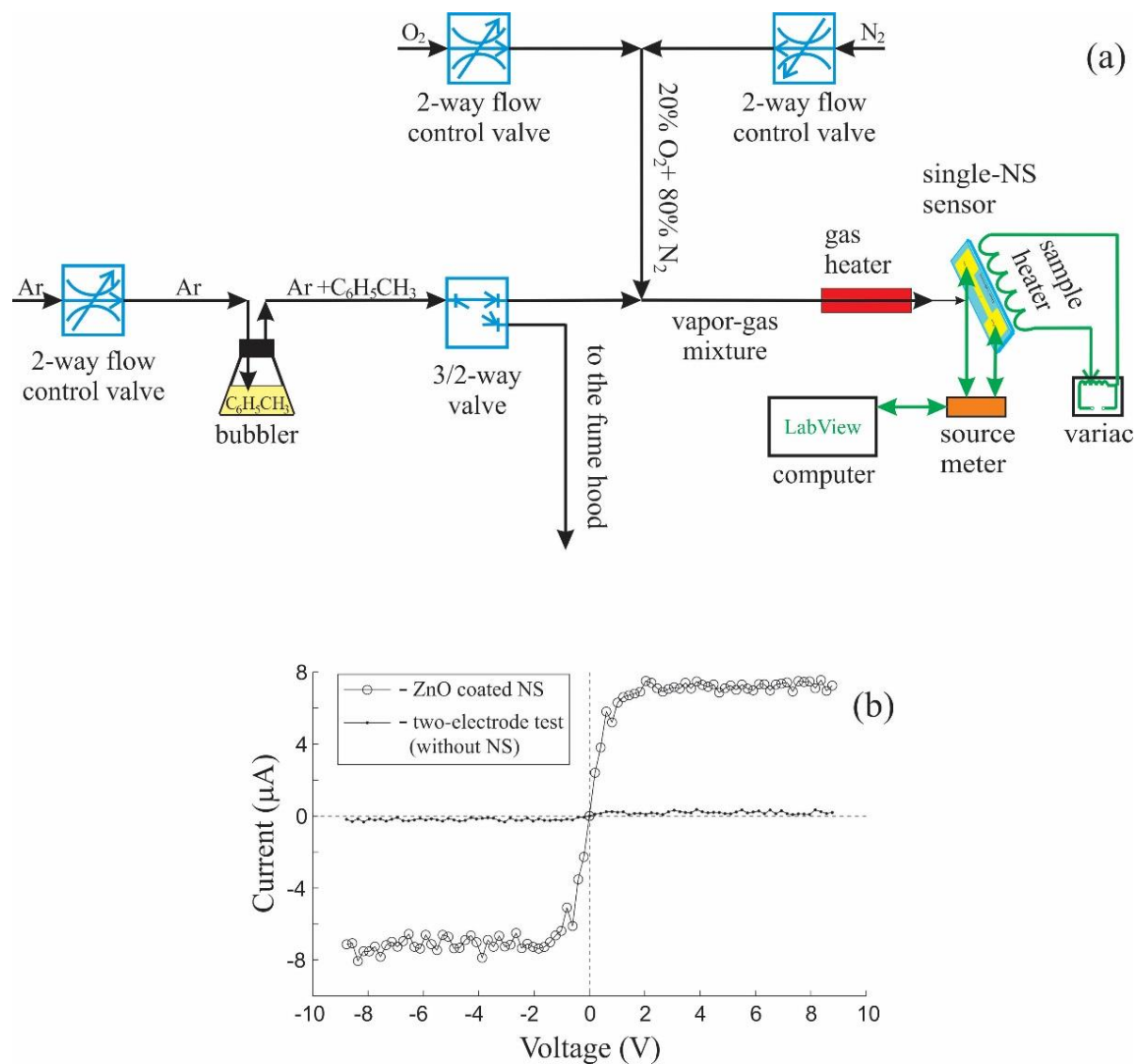


Figure 3.5 (a) Schematic of the two-probe measurement system used to acquire electrical response of individual ZnO coated silica nanospring. (b) I-V characteristics of a single ZnO coated nanospring device and of the electrodes without nanospring at temperature of 300°C.

3.3 Results and Discussion

The electrical response of the single ZnO coated nanospring device to toluene, as a function of sensor temperature (T_{NS}) and vapour-gas mixture (toluene vapor and synthetic air) temperature (T_V), was analyzed to determine the operating conditions under which the ultimate sensitivity can be achieved. The first set of experiments examined the dependence of the electrical chemiresistor response on the sensor temperature (T_{NS}) with a toluene vapor-gas mixture at room temperature. The single nanospring chemiresistor response to 1000 ppm toluene vapor pulses for $T_{NS} = 160^\circ\text{C}$, 270°C , 310°C , and 350°C , are plotted in Figs 3.6 (a), 3.6 (b), 3.6 (c), and 3.6 (d), respectively. At $T_{NS} = 160^\circ\text{C}$ the response is 50% of the baseline, but the signal is prone to noise spikes due to shot and flicker noise, which become significant sources of noise at relatively low temperatures when thermal noise is low [28,29].

As expected, the response increases precipitously at $T_{NS} = 270^\circ\text{C}$, producing a response factor of 28. Further heating to $T_{NS} = 310^\circ\text{C}$ produces the maximum response factor of 48, which drops to 14 at $T_{NS} = 435^\circ\text{C}$. The rise and fall in sensitivity as a function of the chemiresistor temperature is due to two competing processes, namely: generation of free carriers (decreases the resistance) and oxidation of the ZnO surface (increases the resistance). In the oxidation process, chemisorbed oxygen species trap “free” electrons from the near-surface region of the ZnO (redox process) [7,9], i.e. Zn atoms are in the fully oxidized Zn^{2+} state. In addition, thermal activation is needed for electrons to overcome the surface potential barrier and to reach the oxygen species at the ZnO surface. In terms of the chemiresistor response, a negative surface charge is formed, which depletes the n-type ZnO semiconductor layer, thereby increasing the resistance of the film, or ZnO coated nanospring in this case. The reduction in the sensitivity for $T_{NS} > 310^\circ\text{C}$ is attributed to the excitation of surface phonons,

which significantly increases the oxygen desorption rate from the ZnO surface. The maximum chemiresistor response for $T_{NS} = 310^{\circ}\text{C}$ reflects the optimum temperature where a balance exists between the aforementioned processes.

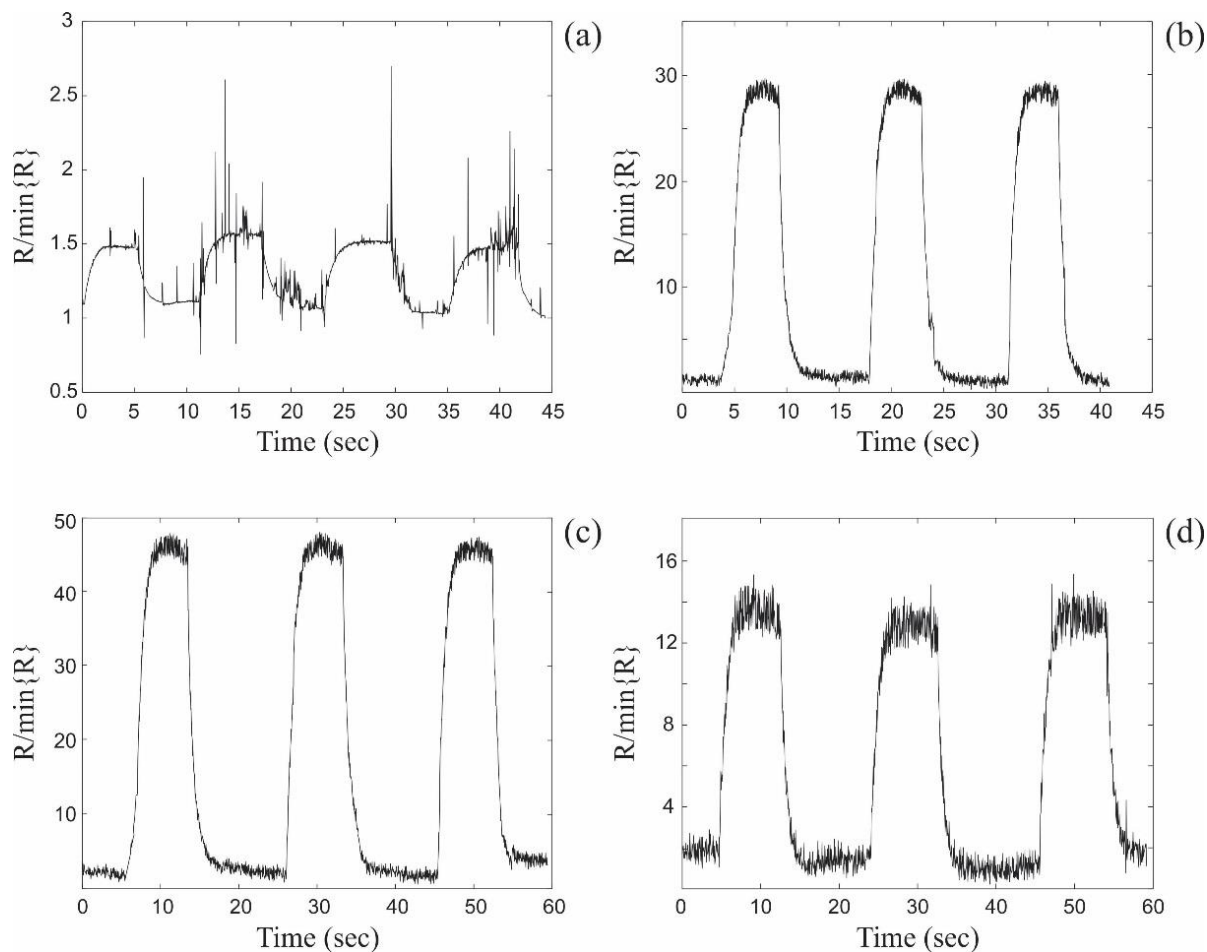


Figure 3.6 The relative changes in resistance of a single ZnO coated nanospring sensor upon exposure to 1000 ppm consequent pulses of toluene vapor at different sensor temperatures T_{NS} (the vapor gas mixture temperature T_V was set around the room temperature). (a) $T_{NS} = 160^{\circ}\text{C}$, (b) $T_{NS} = 270^{\circ}\text{C}$, (c) $T_{NS} = 310^{\circ}\text{C}$, and (d) $T_{NS} = 350^{\circ}\text{C}$.

In the second set of experiments, the response of the single nanospring chemiresistor as a function of the vapor-gas mixture temperature (T_V) at a fixed sensor temperature (T_{NS}) of 310°C was evaluated (Fig. 3.7). The electrical (resistance) response to 1000 ppm pulses of toluene/Ar in the synthetic air was obtained at $T_V = 200^\circ\text{C}$, $T_V = 250^\circ\text{C}$, and $T_V = 300^\circ\text{C}$, are displayed in Figs 3.7 (a), 3.7 (b), and 3.7 (c), respectively. The effect of preheating the vapor-gas mixture produces a large response relative to the room temperature measurements, where a maximum response factor of 100 occurs at $T_V = 250^\circ\text{C}$. At $T_V = 300^\circ\text{C}$, the response drops precipitously to 15, along with a corresponding drop in the signal to noise ratio.

In Chapter 2, it was shown that as a consequence of heating the vapor-gas mixture (synthetic air and toluene vapor), a competition arises between the heating induced increase of the concentration of adsorbed oxygen species and vapor phase dissociation of the toluene. Heating of the synthetic air enables oxygen to activate additional surface sites and enhances the oxygen dissociative chemisorption rate, thereby increasing the concentration of ionic oxygen (O^-) species on the ZnO surface. The higher concentration of O_2^- and O^- on the surface leads to the enhancement of the chemiresistor response (sensitivity) (Figs. 3.7 (a) and 3.7 (b)). On the other hand, the gas heating intensifies the toluene oxidation process in the ambient air prior to reaching the ZnO surface. That, in turn, decreases the toluene oxidation rate at the ZnO surface and reduces the sensitivity (Fig. 3.7 (c)). Ultimately, the highest chemiresistor response/sensitivity with a factor of 100 is achieved at T_{NS} of 310°C and $T_V = 250^\circ\text{C}$. The electrical response of the single ZnO coated nanospring device to toluene at the partial vapor pressures of 60 ppm, 40 ppm, 20 ppm and at the sensor temperature of 310°C (without gas heating) is shown in Fig. 3.8 (a). The chemiresistor exhibits good linearity of the calibration graph (response vs analyte concentration) with a slope of 18% response change per 40 ppm

toluene partial pressure change. Relative changes in resistance of a thin polycrystalline ZnO layer deposited on the flat SiO₂ surface upon exposure to toluene vapor at the partial pressures

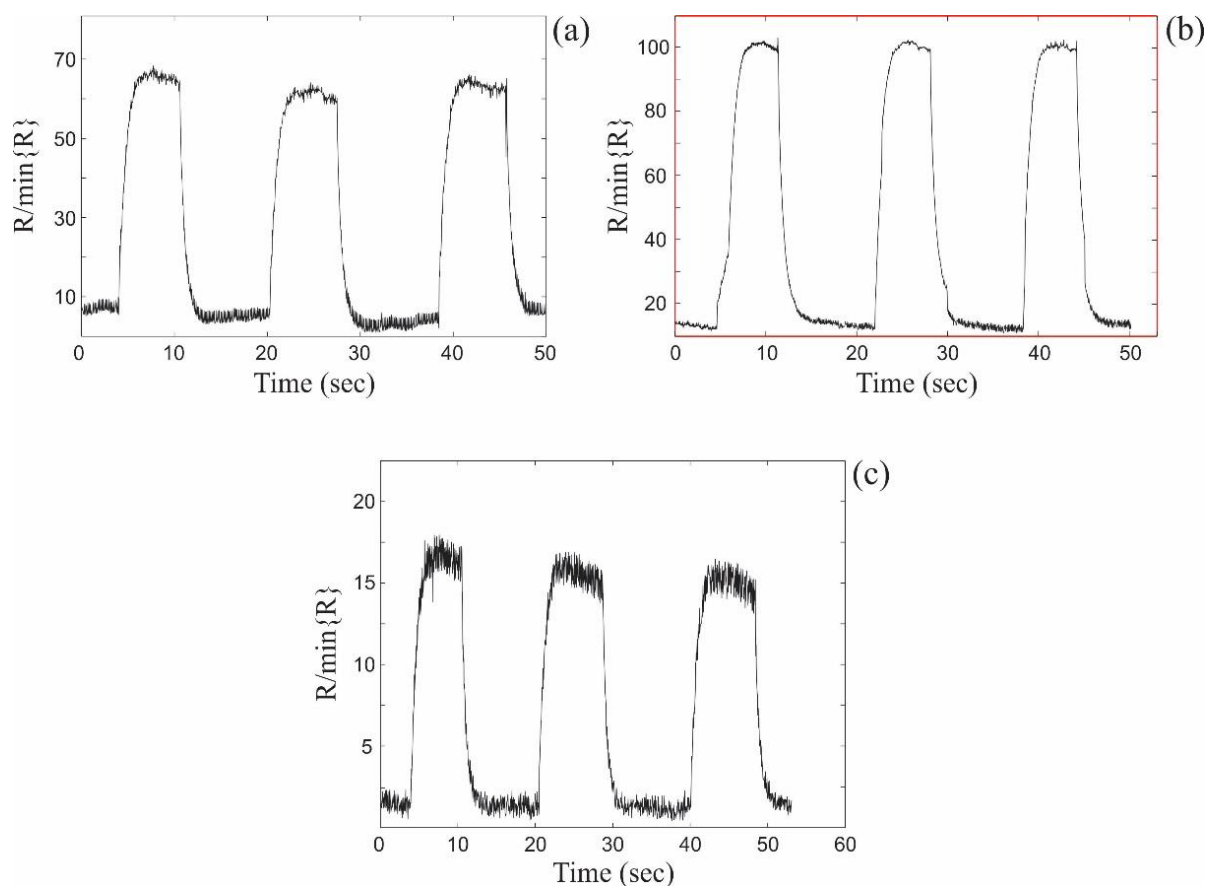


Figure 3.7 The relative changes in resistance of a single ZnO coated nanospring sensor upon exposure to 1000 ppm consequent pulses of toluene vapor at different vapor gas mixture temperatures T_v . The sensor temperature $T_{NS} = 310^\circ\text{C}$. (a) $T_v = 200^\circ\text{C}$, (b) $T_v = 250^\circ\text{C}$, and (c) $T_v = 300^\circ\text{C}$.

of 60 ppm, 40 ppm, 20 ppm and at the ZnO surface temperature of 310°C (without gas heating) are displayed in Fig. 3.8 (b). The extrapolations of the straight calibration lines for the single ZnO coated nanospring device and for the ZnO layer on the SiO₂ wafer are presented in Fig. 3.8 (c). These linear extrapolations of the calibration curves correspond to the ppm

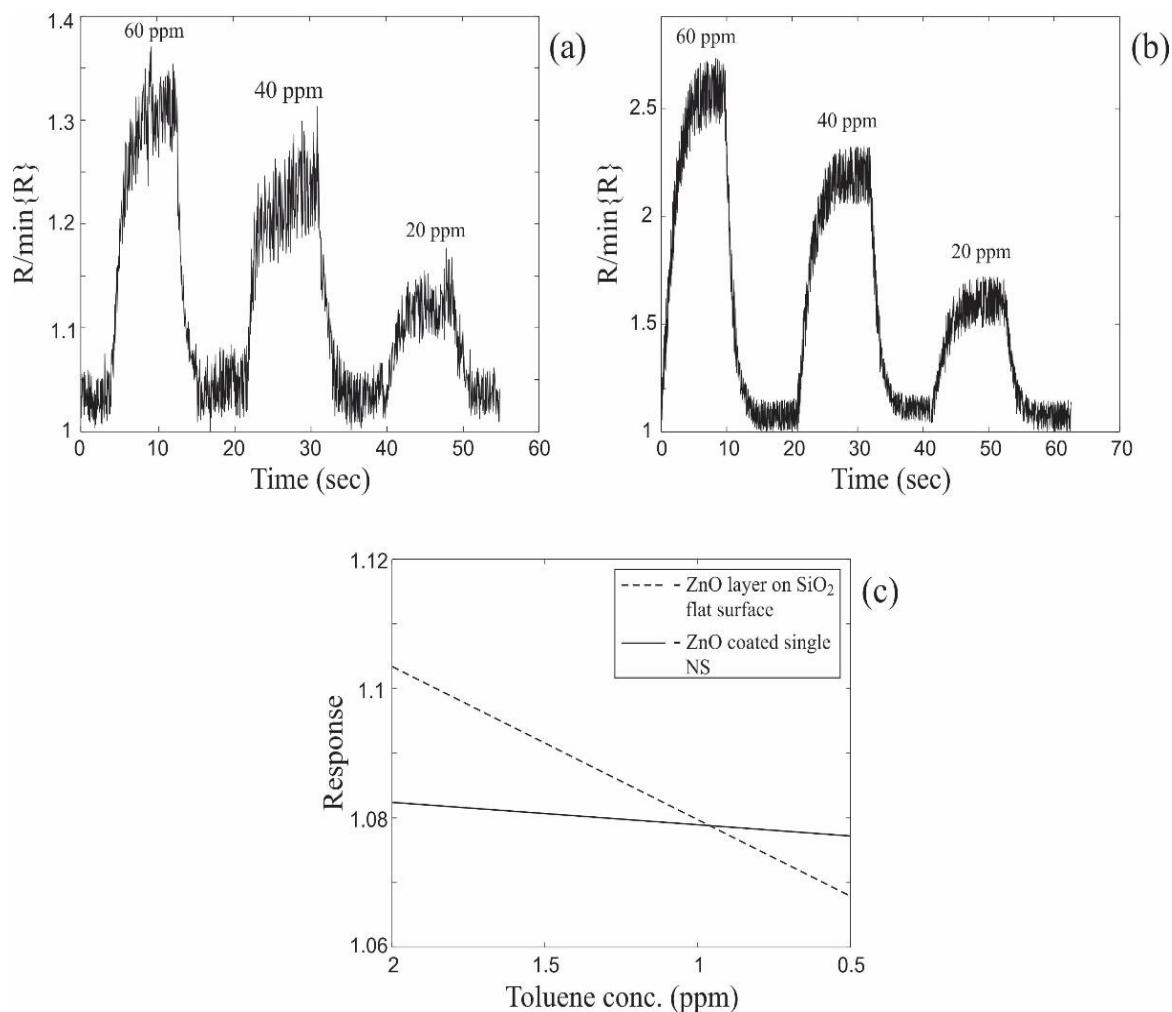


Figure 3.8 (a) The relative changes in resistance of a single ZnO coated nanospring sensor upon exposure to toluene vapor at 60 ppm, 40 ppm, and 20ppm, (b) the relative changes in resistance of a ZnO thin film on a flat SiO_2 surface upon exposure to toluene vapor at 60 ppm, 40 ppm, and 20 ppm and (c) the linear extrapolations of the responses of a single ZnO coated nanospring chemiresistor and the ZnO thin film chemiresistor as a function of toluene concentration.

concentration level only. At other concentration ranges, e.g. ppb and ppt, different slopes are expected. The coefficients of determination, R^2 , of the linear extrapolations in Fig. 3.8 (c) have been estimated as 0.74 and 0.76 for the single nanospring device and for the ZnO layer

on the SiO₂ wafer in the ppm range, respectively. The electrical response measurements conducted at the ppb level for nanospring based sensors were performed and thoroughly described in our papers [3-5]. The ZnO layer on a SiO₂ wafer demonstrates a greater slope of the calibration graph and a higher sensitivity at the toluene vapor concentrations of the ppm level (Fig. 3.8 (b)) than the single ZnO coated nanospring device. However, at the ppb level, ZnO coated nanospring based chemiresistors (both a single nanospring device and a nanospring mat samples [2-4]) show a higher sensitivity in terms of electrical response and a lower detection limit than flat ZnO layers Fig. 3.8 (c)). The interpretation of the results in Fig. 3.8 (c) is that the ZnO thin film chemiresistor will be more responsive over a narrow range relative to the single ZnO coated nanospring chemiresistor. Therefore, if the chemiresistor application is to detect small changes in analyte concentration, then the thin film chemiresistor is the appropriate geometry. In contrast, if the application is to measure the lowest possible concentration of the analyte, the nanospring based chemiresistor is the appropriate geometry. In effect, the parameters governing the application will dictate the choice of chemiresistor geometry.

The similarity in crystal structures of ZnO deposited on the flat SiO₂ wafer and on the silica nanospring mat (see Fig. 3.1) indicates that the difference in gas sensing performance of the ZnO polycrystalline structures grown on the flat SiO₂ surface and on the silica nanosprings stems from the influence of chemiresistor geometry on its sensitivity. It will be demonstrated in the proceeding section that the periodic boundary conditions of the nanospring is responsible for its lower detection limit.

3.4 Computational model

The preferential *c*-axis orientation of the ZnO crystal structure shown in Figures 1(a) and 1(b) can be explained by the “survival of the fastest” model described by Van der Drift [30]. This model states that different crystal planes orientations occur at an early stage of the deposition, while the fastest growing crystal planes out compete the others. In our experiments the fastest growing plane has the (002) *c*-axis orientation.

The quantitative model of the ZnO coating assumes a hexagonal polycrystalline structure with a (002) preferred orientation. The top view of this hexagonal array is schematically illustrated in Figs. 2.9 and 2.10. The structure is electrically modelled as an array of resistors, R_{ij} , corresponding to the interface, or grain boundary, between i^{th} and j^{th} adjacent nanocrystals. These resistances can be defined as

$$R_{ij} = \rho \frac{L_i}{A_{ij}}, \quad (3.1)$$

where L_i is the characteristic size of the i^{th} nanocrystal; A_{ij} is the interface area between the i^{th} and j^{th} nanocrystals; and ρ is the total resistivity of the crystal structure. According to Matthiessen's rule

$$\rho = \rho_{\text{dislocations}} + \rho_{\text{grain boundaries}} + \rho_{\text{impurities}} + \rho_{\text{phonons}} + \dots, \quad (3.2)$$

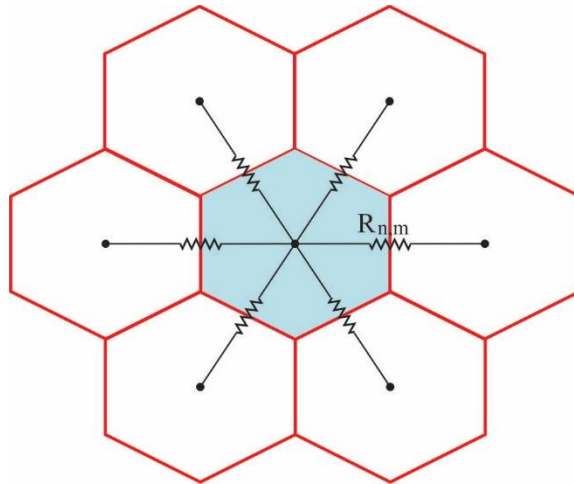


Figure 3.9 Schematics of a hexagonal polycrystalline MOS structure grown with c -axis orientation (top view).

the total resistivity is well described as the sum of resistivities corresponding to different scattering sources presented in a crystalline structure, such as dislocations, grain boundaries, ionized impurity scattering, lattice vibrations (scattering on acoustic and optical phonons), etc. Since there is a distribution of nanocrystals with various characteristic lengths L_i and interfaces areas A_{ij} , we assume that the resistances, R_{ij} , have random values in the range of $R - \delta R$ to $R + \delta R$, where R is an arbitrary chosen average resistance. A well-known Kirchhoff's voltage law approach was used to simulate a DC electrical response of MOS coatings deposited on the surfaces of different geometries. The flat MOS grain structures can be described by the following matrix equation:

$$\hat{\mathbf{R}}^{(F)} \vec{\mathbf{I}}^{(F)} = \vec{\mathbf{V}}^{(F)}, \quad (3.3)$$

where $\hat{\mathbf{R}}^{(F)}$ is the $L \times L$ square resistance matrix with elements R_{ij} ; $\vec{\mathbf{I}}^{(F)}$ is the current vector column of size L ; $\vec{\mathbf{V}}^{(F)}$ is the voltage vector column of size L with only one nonzero element

which corresponds to a constant applied voltage V_a (see Fig. 3.10); and L is the number of loops schematically shown in Fig 3.10. The value of L is approximately equal to the total number of grains in the polycrystalline structure.

The MOS coated 3D structures, such as cylindrical surfaces or nanospring mats, can be described by the linear least squares

$$\hat{\mathbf{R}}^{(3D)}\vec{\mathbf{I}}^{(3D)} = \vec{\mathbf{V}}^{(3D)}, \quad (3.4)$$

where $\hat{\mathbf{R}}^{(3D)}$ is the $(L+N) \times L$ resistance matrix with elements R_{ij} ; $\vec{\mathbf{I}}^{(3D)}$ is the current vector column of size L ; $\vec{\mathbf{V}}^{(3D)}$ is the voltage vector column of size $L+N$ with only one nonzero element, which once again corresponds to a constant applied voltage V_a ; and N is the number of additional linearly independent Kirchhoff's equations. These N equations correspond to additional loops in the electrical circuit; the appearance of these loops arises from the periodicity that the cylindrical cross section of the nanospring imparts on the ZnO coating, i.e. a random distribution of periodic boundary conditions. The additional loop related to the cylindrical structure with axis a is schematically illustrated in Fig. 3.10 (a) by a dash blue line which virtually “connects” the two nodes of the same electrical potential. Hence, N is the number of “connections” present in arbitrary 2D film mapped onto the 3D structure of the nanospring.

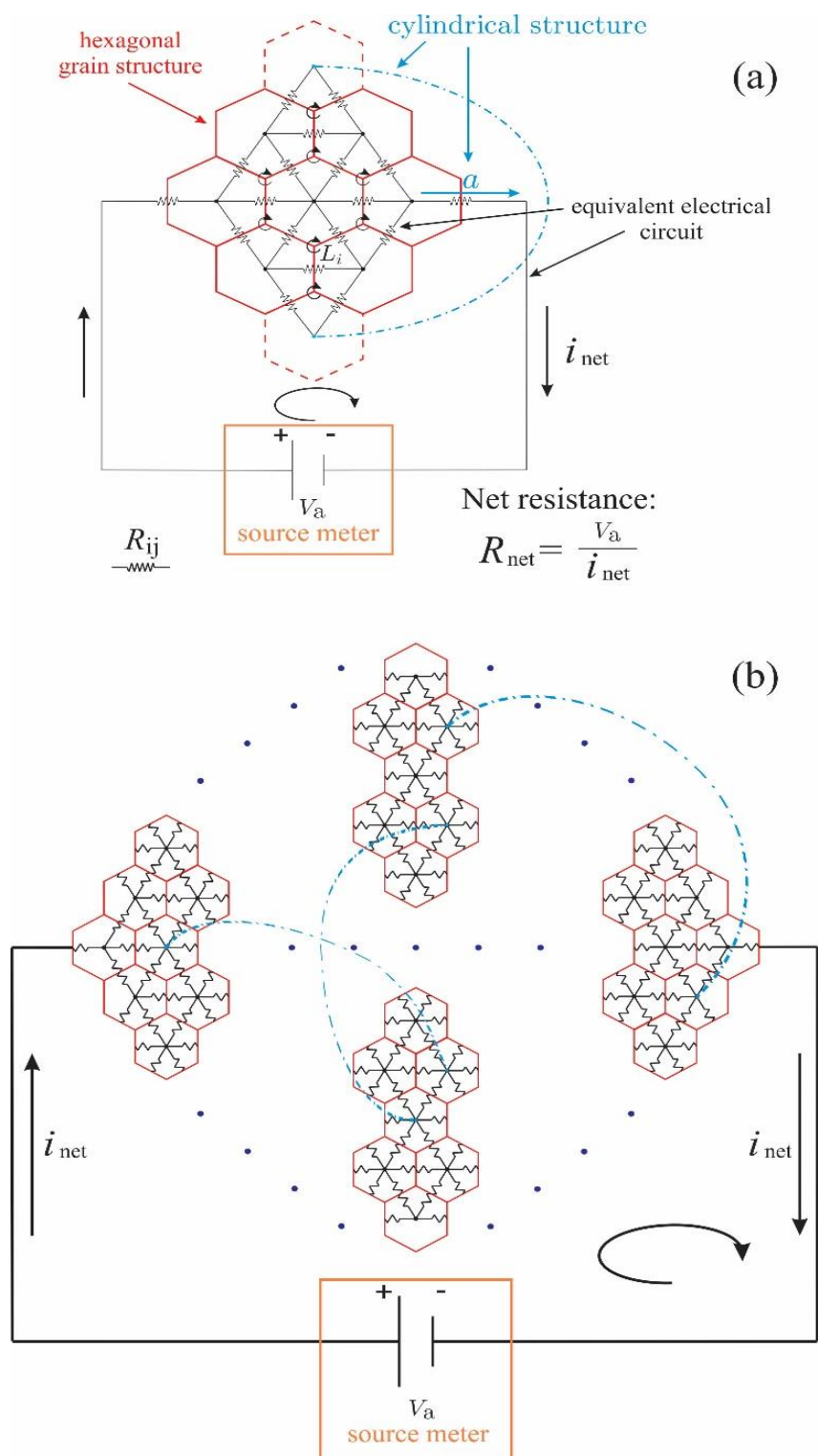


Figure 3.10 Schematics of hexagonal polycrystalline structure with a (002) orientation and its equivalent electrical circuit.

Recalling that the response to toluene vapor is attributed to its oxidation and the corresponding stripping of ionized oxygen species from the ZnO surface [1–5], this, in turn, returns the aforementioned “trapped” electrons back into the bulk, causing a decrease in the potential barrier height at the nanocrystal boundaries and a corresponding reduction of the resistances by δR_{ij} . δR_{ij} are the variables of the model used to tune the degree of response of the resistive elements. For example, for a high analyte concentration, δR_{ij} will be larger than at a low analyte concentration. The relative change in the net resistance R_{net} (see Fig. 3.10) simulates the response of ZnO hexagonal polycrystalline structure to the reactive vapor.

The results of numerical computations for the net electrical responses of the hexagonal polycrystalline structures deposited on flat and on random cylindrical surfaces for three different perturbations of the matrix elements R_{ij} , namely $\delta R_{ij} = 0.1$, $\delta R_{ij} = 0.05$, and $\delta R_{ij} = 0.01$ are illustrated in Figs 3.11 (a), 3.11 (b), and 3.11 (c), respectively.

In figures 7(a)–7(c) the number N is the relative number of additional random loops present in 3D (cylindrical) structure, which is determined by the ratio,

$$N = \frac{N}{N_G}, \quad (3.5)$$

where N_G is the total number of grains in the crystal structure. At $N = 0$ the 3D structure coincides with the flat structure. For the nanospring based systems the relative number N is approximately equal to the ratio of an average characteristic grain size, L_G , to the circumference of the nanospring cross section of an average diameter, D :

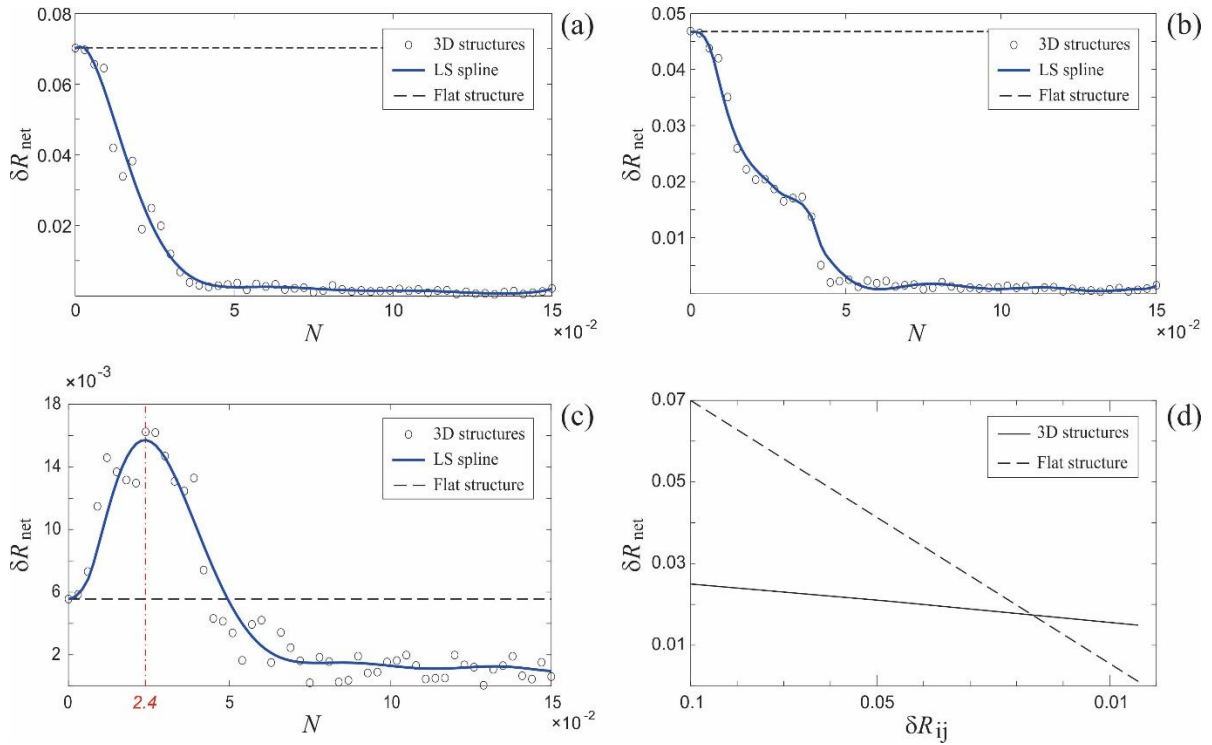


Figure 3.11 Numerical simulations of the relative changes of the measured resistances δR_{net} as functions of N for hexagonal polycrystalline structure on flat and arbitrary 3D structures at different δR_{ij} . (a) $\delta R_{ij} = 0.1$, (b) $\delta R_{ij} = 0.05$, (c) $\delta R_{ij} = 0.01$. (d) Linear approximations of δR_{net} as functions of δR_{ij} for 3D at $N = 0.024$ and flat structures.

$$N = \frac{L_G}{\pi D}. \quad (3.5)$$

The average size of the ZnO nanocrystals of 16 nm was estimated by applying Scherrer's eq. for the XRD data shown in Figs. 3.1 (a) and 3.1 (b). The average nanospring diameter is about 150 nm. Hence, for the single ZnO coated nanospring device $N = 0.034$.

Figs. 3.11 (a) – 3.11 (c) demonstrate that at relatively high perturbations (δR_{ij}) of the matrix elements (see Figs. 3.11 (a), 3.11 (b)), the electrical response, δR_{net} , of the flat polycrystalline structure is greater than the response of the nanospring, while at relatively small perturbations (Fig. 3.11 (c)), the electrical response of the nanospring exceeds that of the flat structure. The highest sensitivity of the nanospring based sensor at small perturbations occurs for $N = 0.024$. The linear approximations of the calibration graphs (response δR_{net} vs perturbations δR_{ij}) of the nanospring (at $N = 0.024$) and for the flat polycrystalline structures are presented in Fig. 3.11 (d). The data in Figs. 3.11 demonstrate that the polycrystalline MOS structures deposited on a flat surface exhibit a higher slope of the calibration graph and are more responsive to relatively high analyte concentrations than a nanospring. On the other hand, for N approaching the value of 0.024, the nanospring will have a higher sensitivity at lower analyte concentrations and an ultimate lower detection limit than the flat structure. There is good agreement between Fig. 3.8 (c) and figure 3.11 (c), where the magnitude of δR_{ij} is analogous to the analyte concentration.

3.5 Conclusions

The first of its kind single ZnO coated silica nanospring redox chemical sensor (chemiresistor) has been constructed, tested and numerically modelled. It has been demonstrated that not only is the electrical response of the sensor dependent on the temperature of the ZnO surface, but also on the temperature of the vapor-gas mixture (synthetic air and toluene vapor). These dependencies can be explained by the fact that both the temperatures (namely, T_{NS} and T_V) impact the concentration and chemical forms (molecular or ionic) of oxygen on the ZnO surface, as well as the toluene oxidation rate in the

ambient atmosphere. The highest sensitivity was obtained at the sensor temperature of 310°C and the vapor-gas mixture temperature of 250°C. The influence of the chemiresistor geometry on its sensitivity has been examined and analyzed by comparing the electrical response characteristics of a MOS polycrystalline structures deposited on a flat surface and on the surfaces of a nanospring, or any arbitrary structure with a cylindrical cross section. Numerical simulations predict that the flat geometry (a polycrystalline ZnO thin film) will be more responsive to small changes in analyte concentration in the appropriate range of concentration, while the cylindrical geometry (a polycrystalline ZnO on the silica nanospring) will exhibit a higher sensitivity at low analyte concentrations, as well as possess a lower ultimate detection limit. The experimental results and numerical simulations provide a roadmap for determining the appropriate choice of sensor design/geometry for the application. Namely, for ultralow analyte concentrations and ultimate lower detection limit, a single nanospring chemiresistor, or a 1D nanostructure with a cylindrical cross section with polycrystalline coating, is the appropriate choice. However, if a large dynamic response in a narrow range is desired, a thin film is the better choice. Finally, it is important to point out that the model of the nanospring can be applied to chemiresistors consisting of a random array of nanosprings, or like 1D nanostructures.

References

- [1] Bakharev, P.; McIlroy, D. The effect of the periodic boundary conditions of a ZnO-coated nanospring on its surface redox-induced electrical response. *Nanotechnology*, 25, 475501 (2014).
- [2] Bakharev, P.; Dobrokhotov, V.; McIlroy, D. A method for integrating ZnO coated nanosprings into a low cost redox-based chemical sensor and catalytic tool for determining gas phase reaction kinetics. *Chemosensors*, 2, pp. 56–68 (2014).
- [3] Dobrokhotov, V.; Oakes, L.; Sowell, D.; Larin, A.; Hall, J.; Kengne, A.; Bakharev, P.; Corti, G.; Cantrell, T.; Prakash, T.; *et al.* ZnO coated nanospring-based chemiresistor. *J. Appl. Phys.*, 111, 044311:1–044311:8 (2012).
- [4] Dobrokhotov, V.; Oakes, L.; Sowell, D.; Larin, A.; Hall, J.; Barzilov, A.; Kengne, A.; Bakharev, P.; Corti, G.; Cantrell, T.; *et al.* Thermal and optical activation mechanisms of nanospring-based chemiresistors. *Sensors*, 12, pp. 5608–5622 (2012).
- [5] Dobrokhotov, V.; Oakes, L.; Sowell, D.; Larin, A.; Hall, J.; Kengne, A.; Bakharev, P.; Corti, G.; Cantrell, T.; Prakash, T.; *et al.* Toward the nanospring-based artificial olfactory system for trace-detection of flammable and explosive vapors. *Sensors and Actuators B: Chemical*, 168, pp. 138–148 (2012).
- [6] Sysoev, V.; Goschnick, J.; Schneider, T.; Strelcov, E.; Kolmakov, A. A gradient microarray electronic nose based on percolating SnO₂ nanowire sensing elements. *Nano Letters*, 7, pp. 3182–3188 (2007).
- [7] Bochenkov, V.; Sergeev, G. *Metal Oxide Nanostructures and Their Applications*, 2nd ed.; Umar, Hahn, Eds., Stevenson Ranch, Calif: American Scientific Publishers, 2010; Volume 3, pp. 31–52 (2010).

- [8] Liu, X.; Cheng, S.; Liu, H.; Hu, S.; Zhang, D.; Ning, H. A survey on gas sensing technology. *Sensors*, 12, pp. 9635–9665 (2012).
- [9] Barsan, N.; Weimar, U. Conduction model of metal oxide gas sensors. *J. Electroceramics*, 7, pp. 143–167 (2001).
- [10] Barsan, N.; Weimar, U. Understanding the fundamental principles of metal oxide based gas sensors; the example of CO sensing with SnO₂ sensors in the presence of humidity. *J. Phys. Condens. Matter*, 15, R813–R839 (2003).
- [11] Gurlo, A.; Bârsan, N.; Oprea, A.; Sahm, M.; Sahm, T.; Weimar, U. An n- to p-type conductivity transition induced by oxygen adsorption on α -Fe₂O₃. *Appl. Phys. Lett.*, 85, doi:10.1063/1.1794853 (2004).
- [12] Ra, H.; Khan, R.; Kim, J.; Kang, B.; Im, Y. The effect of grain boundaries inside the individual ZnO nanowires in gas sensing. *Nanotechnology*, 21, doi:10.1088/0957-4484/21/8/085502 (2010).
- [13] Li, Q.; Gao, T.; Wang, Y.; Wang, T. Adsorption and desorption of oxygen probed from ZnO nanowire films by photocurrent measurements. *Appl. Phys. Lett.* 86, 123117:1–123117:3 (2005).
- [14] Gas'kov, A.; Rumyantseva, M. Nature of gas sensitivity in nanocrystalline metal oxides. *J. Appl. Chem.*, 74, pp. 440–444 (2001).
- [15] Gas'kov, A.; Rumyantseva, M. Materials for solid-state gas sensors. *Inorg. Mater.*, 36, 293–301 (2000).
- [16] Lagowski, J.; Sproles, E.; Gatos, H. Quantitative study of the charge transfer in chemisorption; oxygen chemisorption on ZnO. *J. Appl. Phys.*, 48, doi:10.1063/1.324156 (1977).

- [17] Watanabe, H.; Wada, M.; Takahashi, T. The activation energy for oxygen desorption from zinc oxide surfaces. *Jpn. J. Appl. Phys.*, 4, 945-947, doi: 10.1143/JJAP.4.945 (1965).
- [18] Moseley, P.; Crocker, A. *Sensor materials*; Institute of Physics Pub: Bristol Philadelphia, USA, pp. 72–73 (1996).
- [19] D’Amico, A.; DiNatale, C.; Paolesse, R. Portraits of gasses and liquids by arrays of nonspecific chemical sensors: trends and perspectives. *Sensors and Actuators B*, 68, pp. 324–330 (2000).
- [20] McIlroy, D.; Alkhateeb, A.; Zhang, D.; Aston, D.; Marcy, A.; Norton, M. Nanospring formation—Unexpected catalyst mediated growth. *J. Phys. Condens. Matter*, 16, R415–R440 (2004).
- [21] Wang, L.; Major, D.; Paga, P.; Zhang, D.; Norton, M.; McIlroy, D. High yield synthesis and lithography of silica-based nanospring mats. *Nanotechnology*, 17, S298–S303 (2006).
- [22] McIlroy, D.; Corti, G.; Cantrell, T.; Prakash, T. Method for Manufacture and Coating of Nanostructured Components. U.S. patent No. 11/993,452, 20 (2009).
- [23] George, S.; Ott, A.; Klaus, J. Surface chemistry for atomic layer growth. *J. Phys. Chem.*, 100, pp. 13121–13131 (1996).
- [24] Elam, J.; George, S. Growth of ZnO/Al₂O₃ alloy films using atomic layer deposition techniques. *Chem. Mater.*, 15, 1020–1028 (2003).
- [25] Przeździecka, E. Characterization of ZnO films grown at low temperature. *Acta Phys. Pol. A*, 14, pp. 1303–1310 (2008).

- [26] Guziewicz, E. ZnO by ALD-advantages of the material grown at low temperature. *Acta Phys. Pol. A*, 116, pp. 814–817 (2009).
- [27] Seguin, J.-L.; Gomri, S.; Guerin, J.; Aguir, K. *Science and Technology of Chemiresistor Gas Sensors*; Aswal, Gupta, Eds.; Nova Science Publishers, New York; pp. 351–371 (2007).
- [28] Konczakowska, A.; Wilamowski, B. *Fundamentals of Industrial Electronics*, 2nd ed.; Irwin, Ed, 2011; Volume 1, Ch. 11, pp. 11-1–11-12 (2011).
- [29] Hung, K.; Ko, P.; Hu, C.; Cheng, Y. A unified model for the flicker noise in metal-oxide- semiconductors field-effect transistors. *IEEE Transactions on Electron Devices*, 37 (3), pp. 654– 665 (1990).
- [30] Van der Drift, A. Philips Res. Rep. 22, 267 (1967).

CHAPTER 4

DC vs. Lock-in Amplifier AC Electrical Response Measurements

Bakharev, P.; McIlroy, D. Signal-to-noise enhancement of a nanospring redox-based sensor by lock-in amplification. *Sensors*, 2015, 15, 13110–13120.

Abstract

A significant improvement of the response characteristics of a redox chemical gas sensor (chemiresistor) constructed with a single ZnO coated silica nanospring has been achieved with the technique of lock-in signal amplification. The comparison of DC and analog lock-in amplifier (LIA) AC measurements of the electrical sensor response to toluene vapor at the ppm level has been conducted. When operated in the DC detection mode, the sensor exhibits relatively high sensitivity to the analyte vapor, as well as a low detection limit at the 10 ppm level. However, at 10 ppm the signal-to-noise ratio is 5 dB, which is less than desirable. When operated in the analog LIA mode the signal-to noise ratio at 10 ppm increases by 30 dB and extends the detection limit to the ppb range.

4.1 Introduction

Gas sensors, or chemiresistors, play a critical role in gas and chemical production and high fuel-efficient combustion engines. In addition, they can be used in environmental monitoring [1,2] and to detect hazardous materials, such as explosives vapors [3–9]. Redox-based sensors, or artificial noses, convert chemical information specific to the analyte in question into analytical electrical signals [4–18]. Consequently, they are also excellent scientific tools for molecular interactions at surfaces, be it physisorption or chemisorption. The use of metal oxide nanocrystalline thin films, as well as other more complex nanomorphologies, in the capacity of gas sensitive layers in chemiresistors is well documented [4–18]. These studies have demonstrated that the sensor is more responsive to small changes in surface stoichiometry (oxidation state of the metal) if the dimensions of the thin film, or the size of the nanostructures, of the metal oxide semiconductor (MOS) are comparable to the width of the intrinsic surface depletion layer. [4–18].

A gas sensor systems should be able to promptly and reliably identify (“detect” and “recognize”) the chemical compound, or compounds, of interest under ambient conditions. One approach to achieve this is to construct a sensor (receptor) array from which a multidimensional electrical response pattern, i.e., a recognition pattern, can be assigned to the compounds. Herein, we present a signal processing methodology using lock-in amplification to increase the signal to noise and absolute detection limit of a single ZnO coated silica nanospring redox-based gas sensor.

4.2 Experimental section

Silica nanospring synthesis, ALD ZnO coating technique, and fabrication of a single nanospring device by photolithography were thoroughly described in sections 3.2, 3.2.1, and 3.2.2 of the current dissertation, respectively.

4.2.1 DC measurements

The DC measurements of the electrical response of a single ZnO coated nanospring chemiresistor have been conducted by using the experimental test station shown in Fig. 3.5 (a) (see Ch. 3, section 3.2.3). The DC electrical response of the sensor operated at 310 °C to toluene at the partial vapor pressures of 60 ppm, 40 ppm, 20 ppm, 10 ppm is presented in Fig. 4.1. The chemiresistor exhibits good linearity of the calibration graph (response vs analyte concentration) with a slope of 18% response change per 40 ppm toluene partial pressure change.

The overall noise in the electrical signal illustrated in Fig. 4.1 has multiple sources and, in general, can be subdivided into intrinsic and extrinsic noise sources. There are many sources of intrinsic noise, each having unique characteristics. For DC measurements conducted for the single ZnO coated nanospring device, the intrinsic noise is comprised of three main constituents, which are thermal noise (Johnson-Nyquist noise), shot noise, and flicker ($1/f$) noise [19,20]. Thermal noise is the electronic noise generated by the thermal equilibrium fluctuations of charge carriers. This noise type does not depend on applied voltage. It appears as white noise with power density spectrum given by,

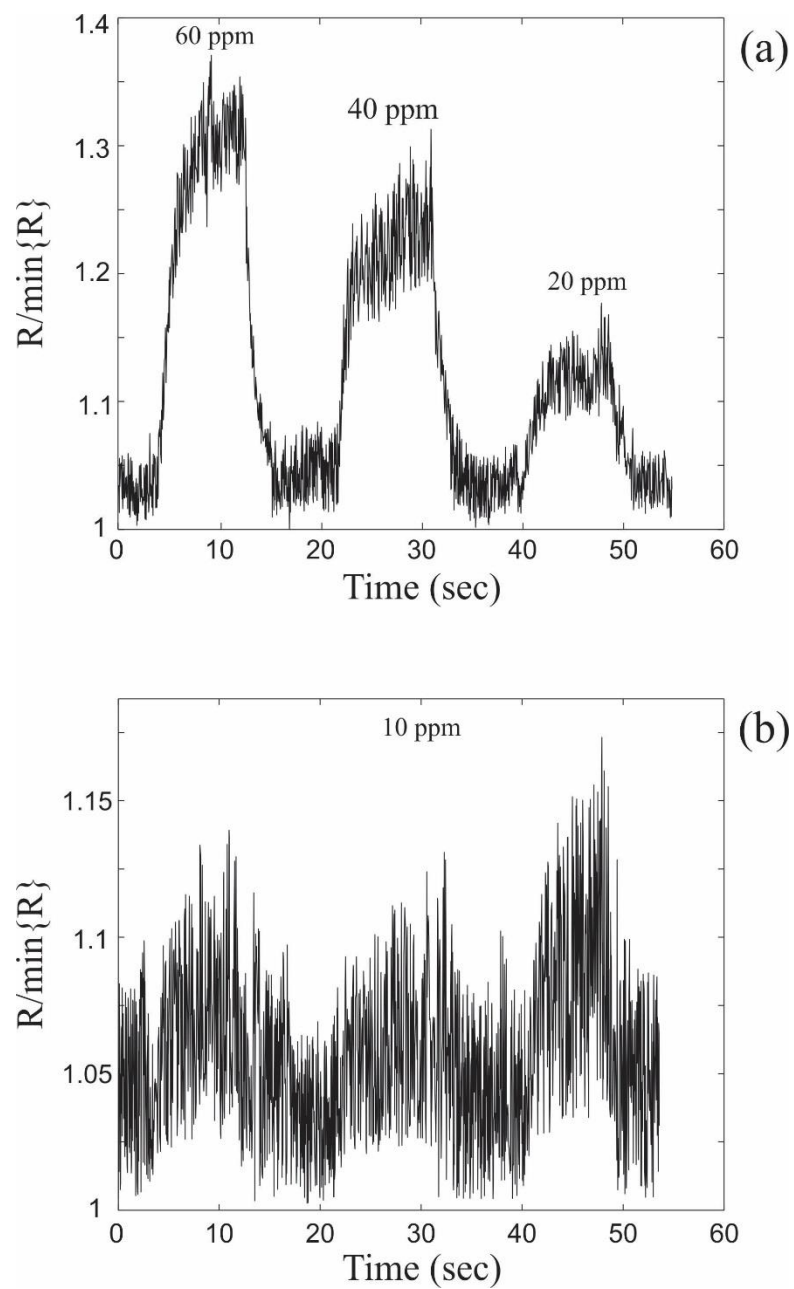


Figure 4.1 DC electrical response of a single ZnO coated nanospring sensor. The relative changes in resistance upon exposure to toluene vapor at (a) 60 ppm, 40 ppm, 20 ppm, and (b) 10 ppm.

$$S_{\text{Th}} = 4k_{\text{B}}T_{\text{NS}}R, \quad (1)$$

where k_{B} is the Boltzmann constant, T_{NS} is the absolute temperature of the sensor, and R is the resistance of the individual ZnO coated nanospring. Heating of the ZnO thermally activates surface sites (such as oxygen vacancies), which subsequently chemisorb atmospheric oxygen. This, in turn, increases the sensor resistance R . Hence, according to equation (1), at elevated temperatures the thermal noise prevails over other intrinsic noise sources.

With that said, shot noise and flicker ($1/f$) noise can become dominant sources of noise at low temperatures with diminished thermal noise (see Fig. 3.6 (a) in Ch. 3) [5]. Shot noise is a white noise source associated with the discreteness of the electric charge with a power density spectrum, S_{Shot} , given by,

$$S_{\text{Shot}} = 2eI, \quad (2)$$

where e is the electron charge and I is the average current in the device. Shot noise can be observed in electronic devices with internal potential barriers, such as potential barriers formed at the crystal grain interfaces and Schottky contacts.

Two major theories have been developed to explain the physical origin of flicker ($1/f$) noise in MOS devices, namely, the number fluctuation theory (NFT) [21–23] originally proposed by McWhorter [24] and the bulk mobility fluctuation theory (MFT) based on Hooge's model [25]. According to the NFT, flicker noise arises from random trapping and detrapping of carriers at defects near the MOS surface and near the MOS/insulator interface (ZnO/SiO₂ interface in this study). Hence, this type of noise can be observed mainly in nanoscale MOS devices with a high surface-to-volume ratio, which is the case for ZnO coated nanosprings. The mobility fluctuation theory attributes the $1/f$ noise to fluctuations in bulk

mobility caused by phonon scattering. According to Hooge's empirical relation, the power density spectrum S_{FI} can be expressed as

$$S_{FI} = \alpha_H \frac{V^2}{Nf}, \quad (3)$$

where N is the total number of carriers in the semiconductor, V is the applied bias voltage, and α_H , known as Hooge's parameter, is an empirical constant used as the measure of the noise magnitude [25].

Extrinsic noise sources include electromagnetic fields that couple into sensitive circuit (radiative coupling, capacitive coupling, inductive coupling, and conductive coupling), mechanical vibrations that trigger piezoelectric materials such as ZnO thin films [26–28] to generate unintended AC electrical signals, or in the present case, noise from random fluctuations in concentrations of flowing gases and vapors.

4.2.2 Lock-in amplifier AC measurements

In order to significantly increase the signal-to-noise ratio (SNR) and subsequently extend the lower detection limit of a ZnO-coated silica nanospring chemiresistor/sensor, the analog lock-in amplifier (LIA) technique has been integrated into the signal processing of sensor signal (see Fig. 4.2 and Fig. 4.3). The inclusion of LIA changes the operating mode of the sensor from DC to AC through the introduction of a modulated input signal generated by the function generator. The AC electrical response measurements were carried out using a Stanford Research Systems SR510 analog LIA. The measurement scheme of the lock-in based experimental set-up used to detect small amplitude modulations in AC signals of the single ZnO coated nanospring chemiresistor is shown in Fig. 4.3 (a).

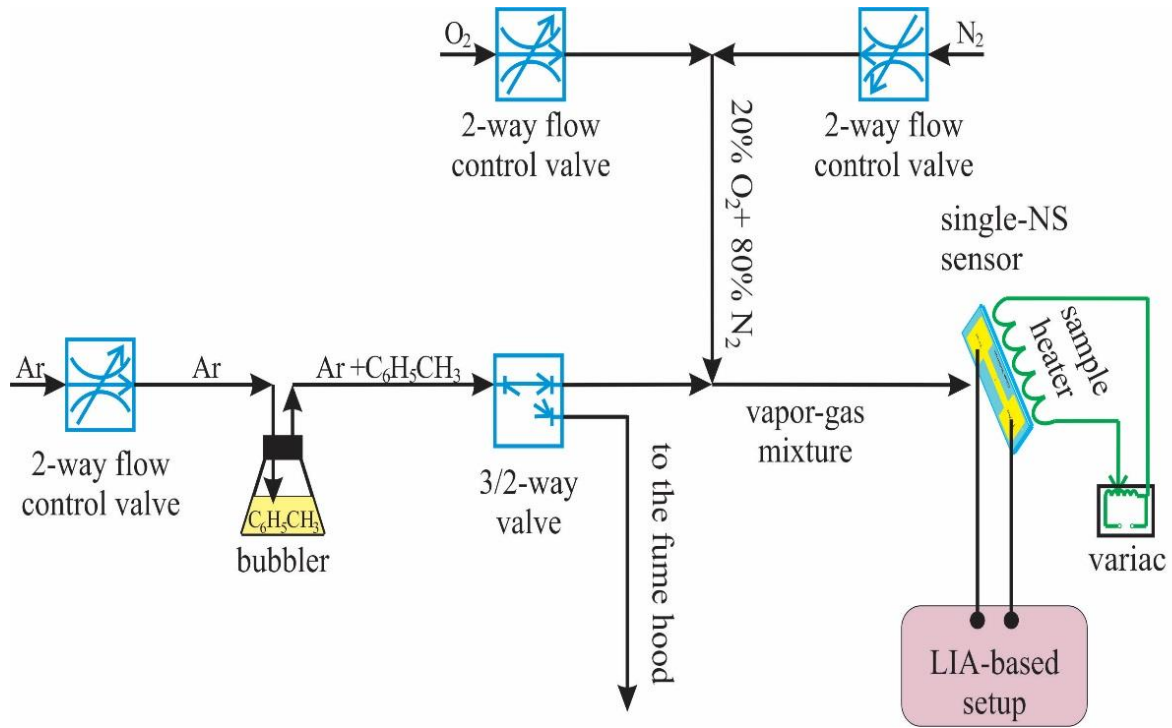


Figure 4.2 A schematic of the gas sensor test station utilized to perform lock-in amplifier AC measurements.

A layout of noisy signal pathway through an analog LIA is illustrated in Fig. 4.3 (b). An input time-dependent signal $s(t; \omega_0)$ in the presence of noise $n(t)$ is multiplied with the reference analog LIA waveform $s_{\text{ref}}(t; \omega_0)$ at the multiplier, also known as the Phase-Sensitive Detector (PSD). PSD generates a signal, the DC component of which is proportional to the amplitude of the AC input signal $s(t)$ and depends on the phase difference between the input signal and the reference signal. The DC component in the PSD output signal can be extracted by means of the low-pass filter (LPF) with the transfer function $H(\omega)$ and the characteristic band-width $\Delta\omega_{\text{LPF}}$. The lock-in quality factor Q can be expressed as

$$Q = \frac{\omega_0}{\Delta\omega_{\text{LPF}}}. \quad (4)$$

The SNR can be defined as the power ratio of a signal to the background noise

$$\text{SNR} = \frac{\overline{P_s(t)}}{\overline{P_n(t)}}, \quad (5)$$

where $\overline{P_s(t)}$ and $\overline{P_n(t)}$ are the average spectral powers of the signal and the background noise, respectively. In decibel scale, the SNR is given as

$$\text{SNR}_{\text{dB}} = 10 \log_{10}(\text{SNR}). \quad (6)$$

The mean square value of the noise amplitude should be used to estimate the experimental SNR, since the background noise is a random signal with zero mean value. The noise obtained from the DC measurements, as well as the noise at the LIA input $n(t)$ with power spectral density $N(\omega)$, can be represented as the following limit:

$$n(t) = \lim_{\Delta\omega \rightarrow 0} \sum_{i=-\infty}^{+\infty} C_i \sin(\omega_i t + \theta_i); \quad \omega_i = i\Delta\omega, \quad (7)$$

where C_i is the Fourier coefficient. Upon the transition through the LIA with the low-pass filter (LPF) transfer function $H(\omega)$, the mean-square value of the output noise is

$$\overline{n_{\text{out}}^2(t)} = \frac{1}{2\pi} \int_{-\infty}^{+\infty} N_{\text{PSD}}(\omega) |H(\omega)|^2 d\omega, \quad (8)$$

where $N_{\text{PSD}}(\omega)$ is the power spectral density of the noise upon passage through the PSD. The transfer function, $H(\omega)$, of the RC low-pass filter (LPF) is,

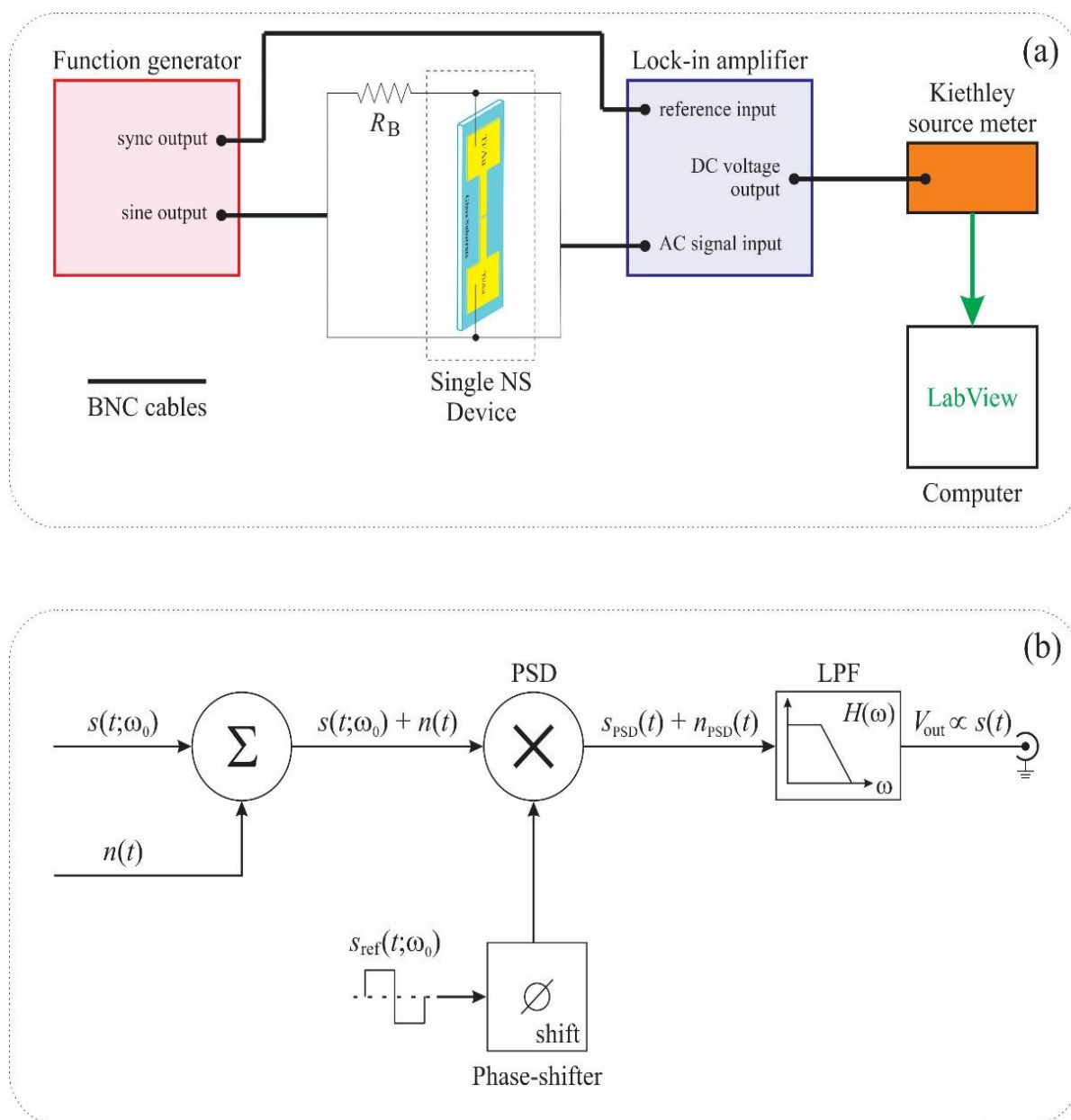


Figure 4.3 (a) Schematic of the lock-in based experimental set-up utilized for toluene vapor detection. (b) Layout of signal pathway through an analog lock-in amplifier (LIA). The symbols Σ and \times represent summing and mixing (multiplying) stages, respectively. PSD and LPF are a multiplier, called the phase sensitive detector, and a low-pass filter with transfer function $H(\omega)$, respectively.

$$H(\omega) = \frac{1}{1 + i\omega\tau_{RC}}, \quad (9)$$

where τ_{RC} is a characteristic time constant of the LPF. Note, the goal of this work is not to identify the dominant noise mode of the chemiresistor, but to increase the SNR. Identification of the degree to which the different types of noise contribute to the signal will be the subject of a future study.

The electrical response of a single ZnO coated nanospring chemiresistor measured at LIA output to toluene vapor pulses at 60 ppm, 40 ppm, 20 ppm, and 10 ppm is displayed in Fig 4.4. The LIA chemiresistor signals in Fig. 4.4 is superior to the DC signals in Fig. 4.1. The contribution of noise to the signal of the chemiresistor in LIA mode is practically negligible down to 20 ppm. At 10 ppm of toluene the signal of the chemiresistor operated in the DC mode is not trustworthy. By contrast, when operated in LIA mode, the chemiresistor signal at 10 ppm is as reliable as that at 60 ppm. Note, there is no loss of information with regards to the amplitude of the signal when operated in the LIA mode. The utilization of the LIA technique significantly improves not only the electrical response characteristics of a single ZnO coated nanospring sensor (receptor) but also considerably expands the recognition capabilities of the gas sensor array (electronic nose) in the frames of linear discrimination analysis (LDA), independent component analysis (ICA), principal component analysis (PCA) and other multiple odor recognition methods [9,11, 28–30]. The repeatability of the signal profile and intensity will greatly increase the reliability of LDA-based detection.

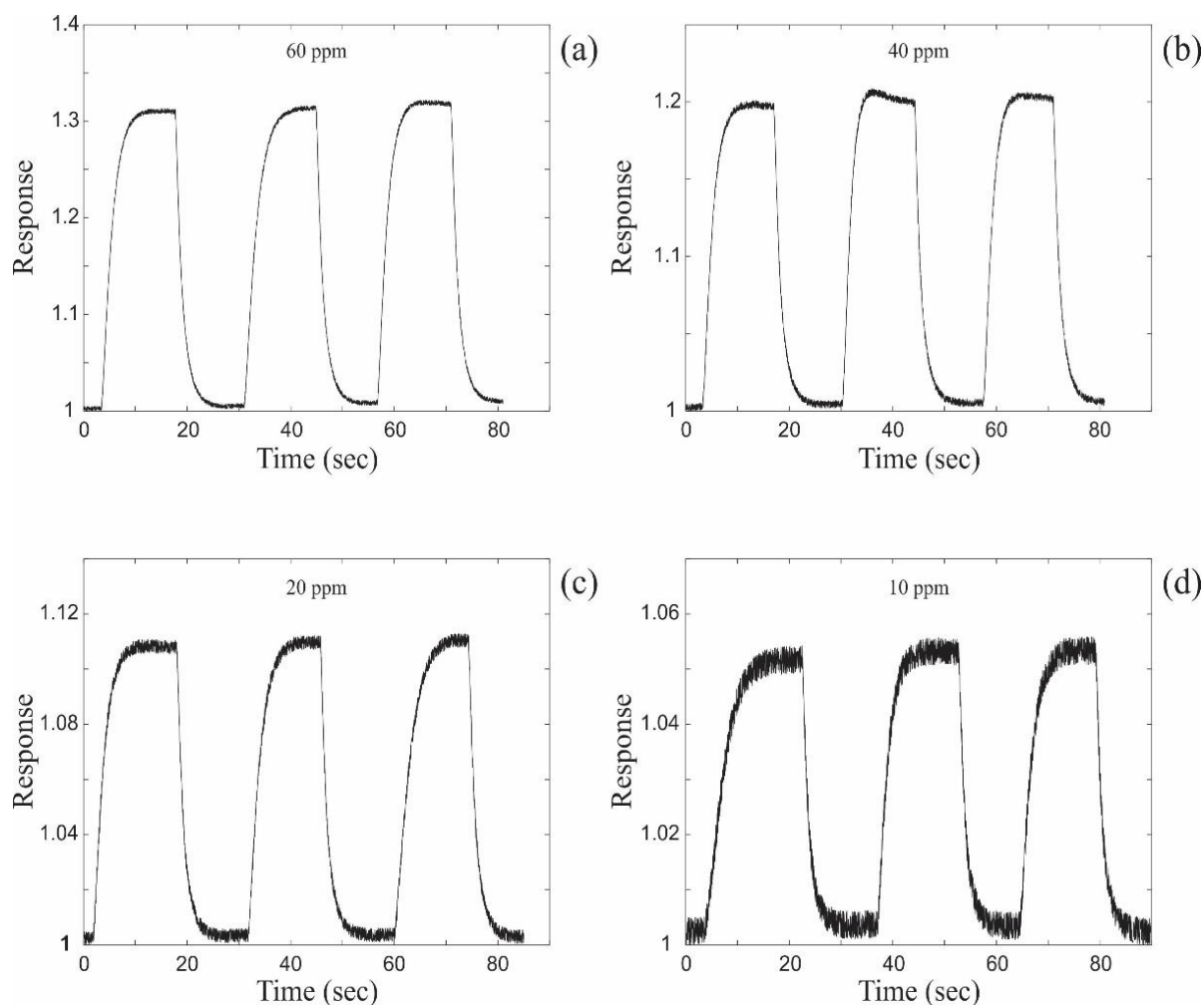


Figure 4.4 The electrical response of a single ZnO coated nanospring device measured at lock-in amplifier (LIA) output upon exposure to toluene vapor at (a) 60 ppm, (b) 40 ppm, (c) 20 ppm, and (d) 10 ppm.

A summary SNR of the chemiresistor operated in DC and LIA modes is presented in Fig. 4.5, which clearly demonstrates the significant increase in the SNR upon signal passage through the LIA at all concentrations. This effect is attributed to the fact that only the low-frequency components of the noise power spectral density, $N_{\text{PSD}}(\omega)$, contribute to the LIA output noise within its equivalent noise bandwidth (ENBW) $\Delta\omega_{\text{LPF}}$. The ENBW, $\Delta\omega_{\text{LPF}}$, of

the RC LPF is approximately equal to $1/\tau_{RC}$. For practical purposes of gas sensors, real-time response measurements are required, so the integration timescale of LIA should be low enough to facilitate relatively short detection response times. Hence, the characteristic time constant, τ_{RC} , of the RC LPF was set to 50 msec since it is much shorter than the sensor response time [5,6] and simultaneously very long compared to the period, T_0 , of the reference signal ($T_0 = 10$ msec). Comparing the SNRs of the DC and LIA measurements performed for a single ZnO coated silica nanospring, the utilization of the conventional analog LIA leads to the sensor resolution reduction of a factor of about 20.

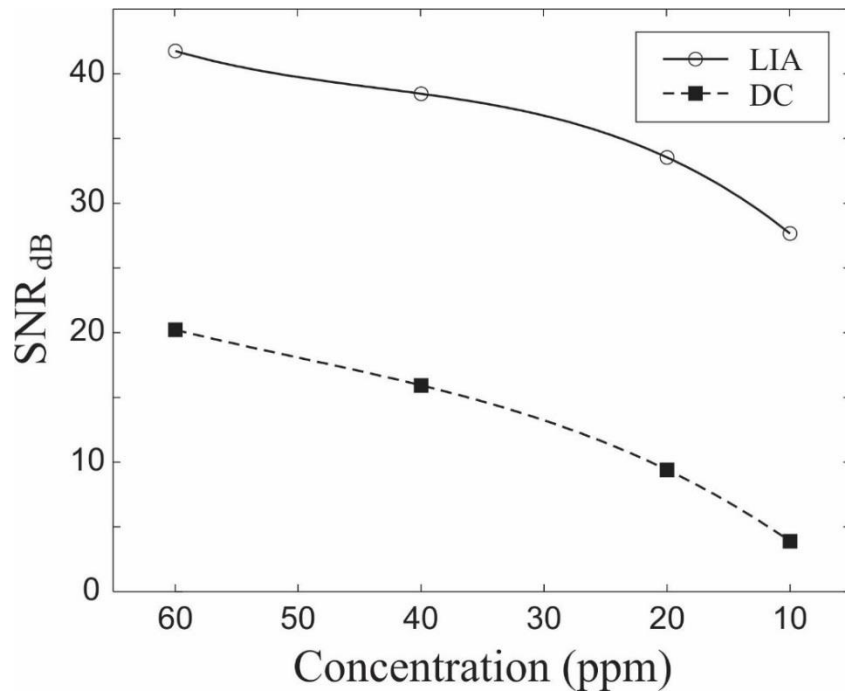


Figure 4.5 Signal-to-noise ratios (SNRs) in decibel scale of a single ZnO coated nanospring sensor obtained by utilizing the DC and the analog lock-in amplifier (LIA) modes of detection.

Hence, the analog LIA measurements of small AC modulation signals generated by the redox and the analyte oxidation processes at the ZnO surface [5–9] enable a detection limit of the sensor to be reduced from tens of ppm (for DC measurements) to tens of ppb range under equivalent experimental conditions.

4.3 Conclusions

A new nanomaterials-based chemical sensor (chemiresistor) that has been developed exhibits excellent sensitivity and SNR. The chemiresistor has been constructed with a single ZnO coated silica nanospring. The gas sensor response to the analyte (toluene) vapor is attributed to its catalytic oxidation of the analyte at the ZnO surface, hence creating an oxygen deficient surface of ZnO, and self-refreshing through dissociative chemisorption of oxygen (redox process). DC mode chemiresistor responses to pulses of toluene vapor at ppm concentration levels demonstrate high sensitivity and a detection limit in the tens of ppm of the single ZnO coated nanospring chemiresistor. By comparison, when the nanospring chemiresistor is operating in the analog lock-in amplifier mode a superior SNR is achieved and the detection limit is extended to tens of ppb. In conclusion, it has been shown that the operation of a chemiresistor operated in the analog LIA mode significantly increases the SNR, improves sensitivity and considerably lowers the detection limit. The LIA operating mode can be used with essentially any chemiresistor, or other types of chemical sensors, especially when employing LDA and ICA signal recognition.

References

- [1] Sekhar, P.; Brosha, E.; Mukundan, R.; Garzon, F. Chemical sensors for environmental monitoring and homeland security. *ECS*, 19 (4), pp. 35–40 (2010).
- [2] Pejcic, B.; Eadington, P.; Ross, A. Environmental monitoring of hydrocarbons: a chemical sensor perspective. *Environmental Sci. and Tech.*, 41 (18), pp. 6333–6342 (2007).
- [3] Bielecki, Z.; Janucki, J.; Kawalec, A.; Mikołajczyk, J.; Palka, N.; Pasternak, M.; Pustelny, T.; Stacewicz, T.; Wojtas, J. Sensors and systems for the detection of explosive devices—An overview. *Metrol. Meas. Syst.*, 19, pp. 3–28 (2012).
- [4] Procek, M.; Stolarczyk, A.; Pustelny, T.; Maciak, E. A Study of a QCM sensor based on TiO₂ nanostructures for the detection of NO₂ and explosives vapours in Air. *Sensors*, 15, pp. 9563–9581 (2015).
- [5] Bakharev, P.; McIlroy, D. The effect of the periodic boundary conditions of a ZnO-coated nanospring on its surface redox-induced electrical response. *Nanotechnology*, 25, 475501 (2014).
- [6] Bakharev, P.; Dobrokhotov, V.; McIlroy, D. A method for integrating ZnO coated nanosprings into a low cost redox-based chemical sensor and catalytic tool for determining gas phase reaction kinetics. *Chemosensors*, 2, pp. 56–68 (2014).
- [7] Dobrokhotov, V.; Oakes, L.; Sowell, D.; Larin, A.; Hall, J.; Kengne, A.; Bakharev, P.; Corti, G.; Cantrell, T.; Prakash, T.; *et al.* ZnO coated nanospring-based chemiresistor. *J. Appl. Phys.*, 111, 044311:1–044311:8 (2012).

- [8] Dobrokhotov, V.; Oakes, L.; Sowell, D.; Larin, A.; Hall, J.; Barzilov, A.; Kengne, A.; Bakharev, P.; Corti, G.; Cantrell, T.; *et al.* Thermal and optical activation mechanisms of nanospring-based chemiresistors. *Sensors*, 12, pp. 5608–5622 (2012).
- [9] Dobrokhotov, V.; Oakes, L.; Sowell, D.; Larin, A.; Hall, J.; Kengne, A.; Bakharev, P.; Corti, G.; Cantrell, T.; Prakash, T.; *et al.* Toward the nanospring-based artificial olfactory system for trace-detection of flammable and explosive vapors. *Sensors and Actuators B: Chemical*, 168, pp. 138–148 (2012).
- [10] Sysoev, V.; Goschnick, J.; Schneider, T.; Strelcov, E.; Kolmakov, A. A gradient microarray electronic nose based on percolating SnO₂ nanowire sensing elements. *Nano Letters*, 7, pp. 3182–3188 (2007).
- [11] Bochenkov, V.; Sergeev, G. Bochenkov, V.; Sergeev, G. *Metal Oxide Nanostructures and Their Applications*, 2nd ed.; Umar, Hahn, Eds., Stevenson Ranch, Calif: American Scientific Publishers, 2010; Volume 3, pp. 31–52 (2010).
- [12] Liu, X.; Cheng, S.; Liu, H.; Hu, S.; Zhang, D.; Ning, H. A survey on gas sensing technology. *Sensors*, 12, pp. 9635–9665 (2012).
- [13] Barsan, N.; Weimar, U. Conduction model of metal oxide gas sensors. *J. Electroceramics*, 7, pp. 143–167 (2001).
- [14] Barsan, N.; Weimar, U. Understanding the fundamental principles of metal oxide based gas sensors; the example of CO sensing with SnO₂ sensors in the presence of humidity. *J. Phys. Condens. Matter*, 15, R813–R839 (2003).
- [15] Gurlo, A.; Bârsan, N.; Oprea, A.; Sahm, M.; Sahm, T.; Weimar, U. An n- to p-type conductivity transition induced by oxygen adsorption on α -Fe₂O₃. *Appl. Phys. Lett.*, 85, doi:10.1063/1.1794853 (2004).

- [16] Ra, H.; Khan, R.; Kim, J.; Kang, B.; Im, Y. The effect of grain boundaries inside the individual ZnO nanowires in gas sensing. *Nanotechnology*, 21, doi:10.1088/0957-4484/21/8/085502 (2010).
- [17] Li, Q.; Gao, T.; Wang, Y.; Wang, T. Adsorption and desorption of oxygen probed from ZnO nanowire films by photocurrent measurements. *Appl. Phys. Lett.* 86, 123117:1–123117:3 (2005).
- [18] Gas'kov, A.; Rummyantseva, M. Nature of gas sensitivity in nanocrystalline metal oxides. *J. Appl. Chem.*, 74, pp. 440–444 (2001).
- [19] Seguin, J-L.; Gomri, S.; Guerin, J.; Aguir, K. *Bases of noise spectroscopy for enhancing metallic oxide gas sensors selectivity*. In Science and Technology of Chemiresistor Gas Sensors; K Dinesh, S Gupta, Nova Science Publishers, Inc.; Ch. 10, pp. 351–371 (2007).
- [20] Konczakowska, A.; Wilamowski, B. *Noise in semiconductor devices*. In Fundamentals of Industrial Electronics, 2nd ed.; D Irwin, CRC Press, Ch. 11 (2011).
- [21] Christensson, S.; Lundstrom, I.; Svensson, C. Low frequency noise in MOS transistors-I theory. *Solid-State Electronics*, Volume 11, 9, pp. 797–812 (1968).
- [22] Bertz, F. Theory of low frequency noise in Si MOST's. *Solid-State Electronics*, Volume 13, 5, pp. 631–647 (1970).
- [23] Hsu, S. Surface state related 1/f noise in MOS transistors. *Solid-State Electronics*, Volume 13, 11, pp. 1451–1459 (1970).
- [24] McWhorter A *1/f noise and germanium surface properties*. In Semiconductor Surface Physics; R Kingston, University of Philadelphia Press, Philadelphia, p. 207 (1957).
- [25] Hooge, F. 1/f noise. *Physica*, Volume 83B, 1976, p. 14 (1976).

- [26] Fan, Z.; Lu, JG. Zinc oxide nanostructures: synthesis and properties. *J Nanosci Nanotechnol.*, 10, pp. 1561–1573 (2005).
- [27] Kanno, I.; Kotera, H.; Wasa, K. Measurement of transverse piezoelectric properties of PZT thin films. *Sensors and Actuators A*, 107, pp. 68–74 (2003).
- [28] Sysoev, V.; Strelcov, E.; Kolmakov, A. *Multidimensional micro-arrays based on metal oxide nanowires for electronic nose application*. In *Integrated Analytical Systems*, Springer, New York, NY, Ch. 15, pp. 465–502 (2013).
- [29] Tripathy, A.; Mohanty, A.; Mohanty, M. Electronic nose for black tea quality evaluation using kernel based clustering approach. *International Journal of Image Processing*, Volume 6, 2, pp. 86–93 (2012).
- [30] Brudzewski, K.; Osowski, S.; Dwulit, A. Recognition of coffee using differential electronic nose, *IEEE Transactions on Instrumentation and Measurement*, vol. 61, 6, pp. 1803–1810 (2012).

CHAPTER 5

Summary

5.1 Conclusions

New techniques for characterization of gas/vapor phase kinetics, surface processes such as gas-surface, vapor-surface interactions and redox processes by utilizing novel gas sensitive structures have been established. The surface interactions have been characterized by using real time sensor electrical response characteristics obtained under well-controlled laboratory conditions.

New methods for building gas sensors (chemiresistors) have been developed. The redox chemiresistors have been constructed by coating insulating silica nanosprings with a ZnO gas sensitive layer by using atomic layer deposition technique. An ultra high surface area gas sensor built from a conventional xenon light bulb by coating it with a 3-D ZnO/nanosprings structure has been utilized as an effective low-cost platform to characterize gas-solid, vapor-solid interactions and redox processes. The single ZnO coated nanospring devices have been fabricated by using standard photolithography and lift-off techniques to minimize the dimensions of the gas sensor elements (receptors) and to analyze the influence of the chemiresistor geometry on its sensitivity.

The optimal operational parameters of the gas sensors have been determined in terms of the temperature of the gas sensitive ZnO layer (working temperature), the temperature of the vapor-gas mixture and the crystal structure of the gas sensitive layer.

An electrical response of the gas sensing devices to the analyte (toluene) vapor is attributed to the catalytic oxidation of the target compound on the metal oxide surface and

corresponding stripping of oxygen species (O_2^- , O^- and O^{2-}) from the surface. The self-refreshing reoxidation of the metal oxide surface at elevated temperatures leads to formation of the surface depletion layer and enables the chemiresistors to return to their baseline conditions. Dependences of the sensor response characteristics (sensitivity, response and recovery time constants) on the ZnO surface and vapor-gas mixture temperatures have been observed and analyzed. Exponential ‘RC-circuit’ approximations of the sensor response and recovery curves have been used to determine activation energies of toluene catalytic oxidation and atmospheric oxygen chemisorption on the ZnO surface. The magnitude of the electrical response of metal oxide semiconductor gas sensors can be maximized by heating vapor-gas mixture, but at the expense of the sensor characteristic recovery time.

The question of sensor sensitivity of MOS nanomaterials and MOS thin films has been addressed. The experimental and computational analyses of the electrical responses of the 3-D (nanospring-based) and flat gas sensing structures show that the complexity and periodic boundary conditions of the nanostructures result in a lower detection limit, while flat MOS structures exhibit higher sensitivity to small analyte concentration fluctuations in a narrow range. Our analysis shows that the productive approach to fabrication of integrated sensors (electronic noses) is to use both the structures (3D and flat geometries) as the receptors for a prompt and reliable detection and recognition of the target chemical compounds.

The comparison of the most common techniques used to measure the electrical response characteristics of gas sensors, namely DC and lock-in amplifier AC measurements, has been conducted. The utilization of the LIA technique significantly improves the signal-to-noise ratio of a sensor device and reduces the absolute detection limit from the ppm to the ppb analyte concentration ranges. Hence, the LIA-based sensor signal recognition technique

expands the capabilities of the gas sensor array (electronic nose) in the frames of a linear discrimination analysis (LDA), an independent component analysis (ICA), a principal component analysis (PCA) and other multiple odor recognition methods.

5.2 Future directions

The ultimate goal of the current research is development of novel ZnO coated silica nanospring-based gas sensor platforms, which can be used efficiently, on the one hand, for detection of hazardous compounds (explosives vapors) and, on the other hand, for characterization of the gas-solid, vapor-solid, gas-vapor interactions and redox processes. The study can be further extended by using other types of metal oxide semiconductor materials (e.g. SnO, SnO₂, TiO₂ etc.) as gas sensitive materials. The methods and results described in this project can be applied to future works on the integration of nanomaterials in sensor arrays (electronic noses) for prompt and reliable detection of various chemical compounds in an ambient environment.

Appendix

Permission from MDPI for the research paper to be used in the current dissertation

Dear Pavel,

Thank you very much for your e-mail. Please feel free to re-use the materials were published in paper <http://www.mdpi.com/2227-9040/2/1/56>

For more information about open access, please visit:

<http://www.mdpi.com/about/openaccess>

Wish you all the best in your research and look forward to our future collaboration.

Best regards,

Linda Wang

Senior Assistant Editor

E-Mail: linda.wang@mdpi.com

Permission from IOP for the research papers to be used in the current dissertation

Dear Pavel Bakharev,

Thank you for your email and for taking the time to seek this permission. When you transferred the copyright in your article to IOP, we granted back to you certain rights, including the right to include the article within any thesis or dissertation.

Please include citation details and for online use, a link to the Version of Record.

The only restriction is that if, at a later date, your thesis were to be published commercially, further permission would be required.

Please let me know if you have any further questions.

In the meantime, I wish you the best of luck with the completion of your dissertation.

Kind regards,

Zora Catterick

Publishing Assistant

IOP Publishing